

Original Articles

Long-term tracking of urban structure and analysis of its impact on urban heat stress: a case study of Xi'an, China



Kaipeng Huo, Rui Qin, Jingyuan Zhao, Xuan Ma*

Department of Architecture, Chang 'an University, China

ARTICLE INFO

Keywords:

Google Earth Engine
Remote sensing
Machine learning
Urban structure
Numerical simulation
Urban thermal stress

ABSTRACT

Rapid urbanization has rapidly transformed the urban thermal environment, significantly impacting the daily lives of urban residents and socio-economic activities. Therefore, analyzing the long-term changes in urban structure and the urban thermal environment is of great importance. This study utilizes the Google Earth Engine (GEE) platform and remote sensing tools, employing Landsat and Sentinel series satellite imagery, and introduces the LCZ classification system to identify and study the dynamic changes in the urban structure of Xi'an City and its central Yanta District in 2009, 2014, 2019, and 2023. The WRF-SLUCM model is used to conduct mesoscale climate simulations for the central area of Xi'an, with WBGT as the thermal stress indicator. Pearson correlation analysis is employed to explore the long-term relationship between the thermal environment and urban structure in the study area.

The results show that from 2009 to 2023, the area of built-up land types in Xi'an rapidly increased. The expansion trend is characterized by the rapid spread of LCZ4 to the northern and southern parts of the city, accompanied by a large-scale reduction of LCZ6. The shape and area of the high-temperature zones in Yanta District did not change significantly. However, from 2009 to 2023, the proportion of open high-rise, open mid-rise, and dispersed buildings in Yanta District continued to increase, while the proportion of compact high-rise, compact mid-rise, single-layer dense buildings, and heavy industrial buildings continued to decrease. This indicates a trend of increasing height and decreasing density in the urban structure of the central area of Xi'an over time. Numerical simulation results show that over time, temperature, wind speed, and WBGT in Yanta District exhibited a downward trend, while humidity increased. The average daily temperature decreased by 0.35 °C, average humidity increased by 0.34 g/kg, average wind speed decreased by 0.36 m/s, and average WBGT decreased by 0.25 °C. Correlation analysis results indicate that LCZ7, LCZ8, LCZ10, and LCZ6 are significantly positively correlated with urban heat stress, while LCZ1, LCZD, and LCZG are significantly negatively correlated with WBGT. LCZ8, LCZ10, LCZ1A, and LCZG have the most significant impact on WBGT, with correlation coefficients of 0.61, 0.44, -0.46, and -0.50, respectively. In future urban planning and development, increasing building height, reducing building density, and decreasing impervious surfaces can improve the comfort and safety of the urban climate. The findings of this study can provide reference for future urban planning and promote the sustainable development of Xi'an.

1. Introduction

Former United Nations Secretary-General Kofi Annan stated during the 2002 World Summit on Sustainable Development that, according to relevant studies, over the next two decades, 55 % of the global population will reside in urban areas, with this figure projected to reach another peak of 68 % by 2050 (Nagendra et al., 2018). However, the rapid growth of urban populations brings about another significant challenge: meeting the increasing social needs, directly leading to rapid

changes in urban land use (Mills, 2007). The surge in global population and urban expansion worldwide has further altered the human living environment. These issues are particularly prominent in China, the United States, and India, where their populations collectively account for 40 % of the global population. On the other hand, urban expansion in these countries peaked from 1990 to 2010, covering 43 % of the global expansion area (Liu et al., 2018). Rapid urbanization has significantly altered urban structures, and as the urbanization process accelerates, urban structures are becoming more diverse. This, in turn, affects urban

* Corresponding author.

E-mail address: mxozil@yahoo.com (X. Ma).

thermal environments, climates, and a range of related phenomena. The transformation of natural landscapes in urban areas into impermeable surfaces profoundly affects urban structures and thermal environments. Therefore, to determine the impact of buildings on climatic phenomena, it is necessary to describe better the characteristics of urban land use and urban structural changes (Wang et al., 2021; Xu et al., 2012; Grimm et al., 2008; Li et al., 2013).

Urban expansion has intensified the intensity of Urban Heat Islands (UHIs) (Weng and Yang, 2004). Lemonsu et al. (2014) pointed out that heatwaves are expected to become more frequent by the end of this century (at least once a year) and last longer, with greater intensity (Lemonsu et al., 2014). Meanwhile, the urban heat island effect often exacerbates the high temperatures reached during heatwaves (Basara et al., 2010). Faced with the combined effects of increasing heatwave frequency and intensity and enhanced Urban Heat Islands (UHI), the mortality rate associated with urban heat has become increasingly concerning. High temperatures have been found to have a substantial impact on heat-related mortality rates among people aged 65 and over in cities worldwide (Hendel et al., 2017).

Over the past few decades, numerous research methods concerning urban structure have emerged. Scholars began studying the internal spatial structures of urban areas and exploring models related to these spaces before the 1950s (Gu et al., 2016). Some scholars have studied urban structural planning from the perspective of urban microclimates and believe that a reliable method is needed to improve urban thermal comfort (Blocken et al., 2012). It is also worth studying whether the structural planning adopted by various research institutions effectively optimizes urban thermal environments (Salata et al., 2016).

The extraction of urban structure is a prerequisite for urban structure research. With the rapid development of scientific technologies such as satellites and electronic computers, many scholars have begun using high-resolution remote sensing data combined with advanced machine learning algorithms for urban structure classification and mapping. In recent years, the use of machine learning algorithms for pixel classification of high-resolution remote sensing images has become a popular trend (Wang et al., 2021; Chen et al., 2022; Kafy et al., 2022; Lin et al., 2023). Statistical classification of remote sensing images is challenging because images obtained from remote sensing platforms have many issues, including high dimensionality, multiple sources of noise, and inherent nonlinearity. Classification, clustering, regression, and dimensionality reduction are the most typical objectives of remote sensing data analysis, and machine learning has been successful in remote sensing classification, regression, and other areas (Sharma et al., 2023). The research conducted by numerous scholars has confirmed that machine learning and deep learning algorithms exhibit relatively superior performance compared to other classification techniques (Li et al., 2023; Breiman, 2001). Furthermore, there has been ongoing controversy regarding which machine learning algorithm is best suited for pixel-based classification. Some research findings indicate that machine learning has been widely applied in remote sensing classification tasks this century, with Random Forest (RF) and Support Vector Machine (SVM) being the most suitable machine learning algorithms for Local Climate Zone (LCZ) classification to date (Gao et al., 2020; Puissant and Weber, 2002). The Random Forest (RF) algorithm has been widely applied across multiple domains, while support vector machines (SVMs) have been prominently applied in land cover/use classification, ecosystem and environmental assessment, and built-up infrastructure identification. In land use and cover classification, CNN, RF, and SVM dominate (Puissant and Weber, 2002). The RF algorithm is an emerging highly accurate machine learning algorithm widely used in various classification and regression tasks (Huang et al., 2017). The algorithm has advantages such as simple implementation, high accuracy, and strong resistance to overfitting (Wang et al., 2022).

Chen et al. (2022) combined urban land classification standards to identify different functional zones within cities, inferred surface temperatures using Landsat 8 remote sensing images, and evaluated the

contributions of different types of urban functional zones to the urban thermal environment using the Random Forest algorithm. Xu et al. (2024) assessed the role of high-resolution remote sensing technology in providing reliable and valuable information for urban planning, monitoring, and management, as well as its additional functions in studying urban environments in the future. Zhang et al. (2023) used high-resolution remote sensing images combined with machine learning classifiers to divide the study area into seven types: forests, shrublands, grasslands, farmlands, urban construction land, water bodies, and wasteland. Wang et al. (2023) analyzed the spatiotemporal changes in surface heat islands of eight cities with populations exceeding 5 million using remote sensing data combined with a Random Forest classifier.

Wang et al. (2024)'s recent research has made significant contributions to the fields of machine learning and global environmental issues. In 2020, these scholars applied machine learning methods to study urban heat environment issues. In their first study of 2023, they used artificial neural networks to predict changes in land use efficiency (LULC) and surface temperature in Wuhan, exploring the correlation between surface temperature and carbon emissions in the city. They found that urban expansion is inevitable, and the resulting carbon emissions have a significant correlation with surface temperature (Zhang et al., 2024). In another study published in the same year, they predicted surface temperature in Guangzhou and analyzed the contribution of urban wind environments to surface temperature (Zhang et al., 2024). In their latest 2024 research, they employed various machine learning methods to capture the impact of global land surface temperature (LST) changes on gross primary production (GPP), finding that the random forest model was the most effective (Dymond et al., 2001). In the same year, they used the emerging Long Short-Term Memory (LSTM) model for large-scale studies of urban structure and heat environment changes in the Pearl River Delta urban agglomeration. The results indicated that, without effective cooling measures, the summer maximum temperature in the region could reach 44.6 °C, with high-temperature areas potentially covering 83.64 % (Lambin et al., 2001). Similar findings were also obtained in their research on Nanjing (Wu and Wu, 2023). These studies by the aforementioned scholars demonstrate that the use of machine learning to study urban heat environment issues is an emerging method that has now matured and is widely accepted.

Remote sensing technology is the only method capable of comprehensively and directly monitoring land at regional and national scales (Awuah et al., 2018). High-resolution remote sensing data has gradually become a powerful tool for urban structure identification, urban land use and land cover identification, and research on urban climates and thermal environments, providing practical bases for urban structure planning and management (Wang et al., 2021; Wu et al., 2014; Heiden et al., 2012; Stewart and Oke, 2012; Nikolopoulou and Lykoudis, 2006; Tseliou et al., 2010) (supplementary remote sensing and thermal environment research). However, the term "urban" does not have a single and objective meaning. With the coexistence of traditional and non-traditional land uses and the continuous flow of personnel, capital, commodities, and information between urban and rural areas, urban forms are becoming increasingly decentralized and decentralized, and the boundaries between urban and rural landscapes are often blurred, making it difficult and confusing to classify the structure and land cover types of cities and surrounding areas. To address this issue, Oke (Ali-Toudert and Mayer, 2006) developed an urban classification system—Local Climate Zone (LCZ), which consists of 17 standard LCZs, 15 defined by surface structures and covers, and two defined by building materials and anthropogenic heat emissions. The standard set is divided into "building types" 1–10 and "surface cover types" A, and this study intends to introduce this classification system as a reliable basis for studying urban structure.

In recent decades, there have been two methods for evaluating outdoor thermal comfort: field measurements and numerical simulations (Gál and Kántor, 2020; Sharmin et al., 2017; Arnfield, 2003). Outdoor thermal comfort involves a large number of urban variables and

processes. Although field measurements can provide highly accurate data, they are expensive and time-consuming tasks and can only display the thermal environment of specific locations and times. In addition, urban microclimates are complex systems based on various parameters involving numerous natural and urban processes. Urban microclimate models are susceptible to natural parameters such as temperature, humidity, wind speed, and solar radiation. Therefore, numerical methods have clear advantages over field measurements, as the performance of the former is controlled by multiple variables and processes (Arnfield, 2003; Zhu et al., 2007; Huang et al., 2014). Arnfield (Musy et al., 2015) pointed out that numerical simulations are becoming increasingly popular and excellent for dealing with complex urban climate systems. With the advantages of numerical simulation and the continuous development of personal computer computing capabilities, some simulation tools have emerged to help assess the impact of various urban structures on microclimates and outdoor thermal comfort (Arnfield, 2003; Powers, 2007; Kusaka et al., 2001; McRae et al., 2020). This study plans to use the Weather Research and Forecasting (WRF) model as a numerical simulation tool. The Weather Research and Forecasting (WRF) model is a new generation of mesoscale weather simulation systems that can be effectively used for basic atmospheric research and weather forecasting. The Weather Research and Forecasting (WRF) model is one of the most advanced numerical weather prediction systems currently available and is a modeling tool suitable for mesoscale weather simulation. Considering the influence of urban canopy on mesoscale climate simulation, coupling single-layer urban canopy models (SLUCM) with the WRF model can estimate the energy transfer between the urban surface and the atmosphere and provide reliable urban regional simulations (Mughal et al., 2020; Zhou et al., 2022).

In 2020, Smithson and Adams (2024) used WUDAPT-based LCZ classification maps and various simulation software, including WRF-SLUCM, to study the changes in the thermal environment of San Jose, California. Based on previous research and established methods, this study developed a novel approach for investigating urban thermal environments. In the same year, Zhang et al. (2022) applied a similar methodology to examine urban land use/land cover data and the urban heat island issue in Singapore. The results indicated that, without intervention, future urban density and temperatures in Singapore are expected to rise significantly, highlighting the importance of density restrictions in maintaining thermal comfort in the future. In 2022, Zhang et al. (2022) explored the impact of vehicle heat release on urban heat mitigation in Sendai, Japan, by combining urban LCZ and the WRF model. They further developed a feasible and reliable workflow to quantitatively assess changes in the urban thermal environment at high spatial resolution. In 2024, Zhao et al. (2019) used WRF-SLUCM and WUDAPT- based LCZ fine-scale urban structure classification maps to study the impact of urban expansion on the thermal environment in the Salt Lake Basin. The results showed that future urban growth is likely to increase nighttime surface temperatures by approximately 5–10 °C compared to current urban conditions. These studies demonstrate that high-resolution LCZ urban structure classification maps and the WRF model provide a novel and effective method for studying urban thermal environment issues. Moreover, the continuous improvements made by previous researchers to this methodology suggest that it is still evolving, being applied, and updated.

This study innovatively utilizes the GEE platform to generate LCZ maps, overcoming the complexity and difficulties of traditional GIS platforms in remote sensing data processing. Additionally, it employs machine learning classification methods as a replacement for conventional classification approaches and incorporates Sentinel satellite imagery, offering a more accurate and convenient method for LCZ mapping. Furthermore, the proposed approach makes long-term tracking of urban structural changes more feasible. The analysis of long-term changes overcomes the limitations of single-time-point studies common in previous research, thereby enhancing the stability and reliability of the analysis results.

The structure and process of this study are presented in (Fig. 1). This study plans to introduce the LCZ classification system as a classification standard for urban structure identification. Firstly, due to the unavailability of high-resolution historical image data on the Google Earth Engine (GEE) platform, high-resolution remote sensing historical images combined with Landsat (30 m resolution) images are cropped, stitched, and preprocessed in the ArcGIS workspace. The maximum likelihood classification (MLC) method divides the study area data into 17 LCZs for the years 2009 and 2014 (Wang et al., 2021). Subsequently, on the GEE platform, high-resolution remote sensing data are acquired and pre-processed, and the Random Forest classification method is used to divide the study area data into 17 LCZs for the years 2019 and 2023. Xi'an, Shaanxi Province, is chosen as the study area, and the accuracy of the classification results is validated using a confusion matrix. Combining with Wet Bulb Globe Temperature (WBGT), the WRF-SLUCM model is utilized to simulate and evaluate the interactions and impacts between various LCZ types and the urban thermal environment at the mesoscale, aiming to identify suitable types that can significantly improve the urban thermal environment and outdoor thermal comfort.

The objectives of this study are: (1) to analyze the changes in urban structure in Xi'an over the past 20 years by longitudinally tracking remote sensing data; (2) to further validate the feasibility of the LCZ classification system in urban structure identification; (3) to study the relationship between the changes in urban structure in Xi'an and the urban thermal environment through numerical simulation; (4) to determine LCZ types that can improve urban thermal environment and outdoor thermal comfort as practical bases for future urban structure design and building technology science. The final section provides a summary and conclusion.

2. Research methods

2.1. Study area and data

Xi'an, also known as Chang'an is located in China's geographical center. It has a continental monsoon climate with distinct cold and warm seasons, with an average annual temperature of 13.7 °C. Throughout the several thousand years of civilization and historical development in China, Xi'an was selected as the capital of 13 dynasties (Demuzere et al., 2019). Simultaneously, it is a mega-city situated at the geographical center of China (Fig. 2), surrounded by mountains and plains of varying heights. Xi'an is characterized by flat terrain, with the urban area covering nearly 10,000 square kilometers, including a main built-up area of over 1,000 square kilometers, with an average elevation of about 410 m. Surrounded by the Loess Plateau and Qinling Mountains, it exhibits basin-like geographical features. Geoclimatically, Xi'an falls into the warm temperate semi-humid continental monsoon climate zone, with distinct four seasons and cool, changeable weather in spring and autumn. The average annual temperature is approximately 13.7 °C, with daytime temperatures averaging above 30 °C in summer. According to the climate zone classification for architectural thermal design requirements by the Chinese Ministry of Housing and Urban-Rural Development, Xi'an belongs to the cold region. However, in recent years, intolerable high temperatures in summer in Xi'an have been on the rise, with increasingly frequent extreme high-temperature weather events. Due to its basin-shaped terrain, most of the time, the main urban area of Xi'an experiences calm winds, leading to a low wind-speed environment throughout the year. Therefore, weak atmospheric circulation struggles to dissipate the accumulated heat near the city surface (Wang et al., 2019).

Cloud cover and weather are important factors affecting remote sensing data. Therefore, this study's remote sensing data filter selected clear days with no cloud cover: cloud cover <10 %. Table 1 shows some basic information about the study data, including the type of remote sensing images, start and stop times, and scene cloud cover percentage.

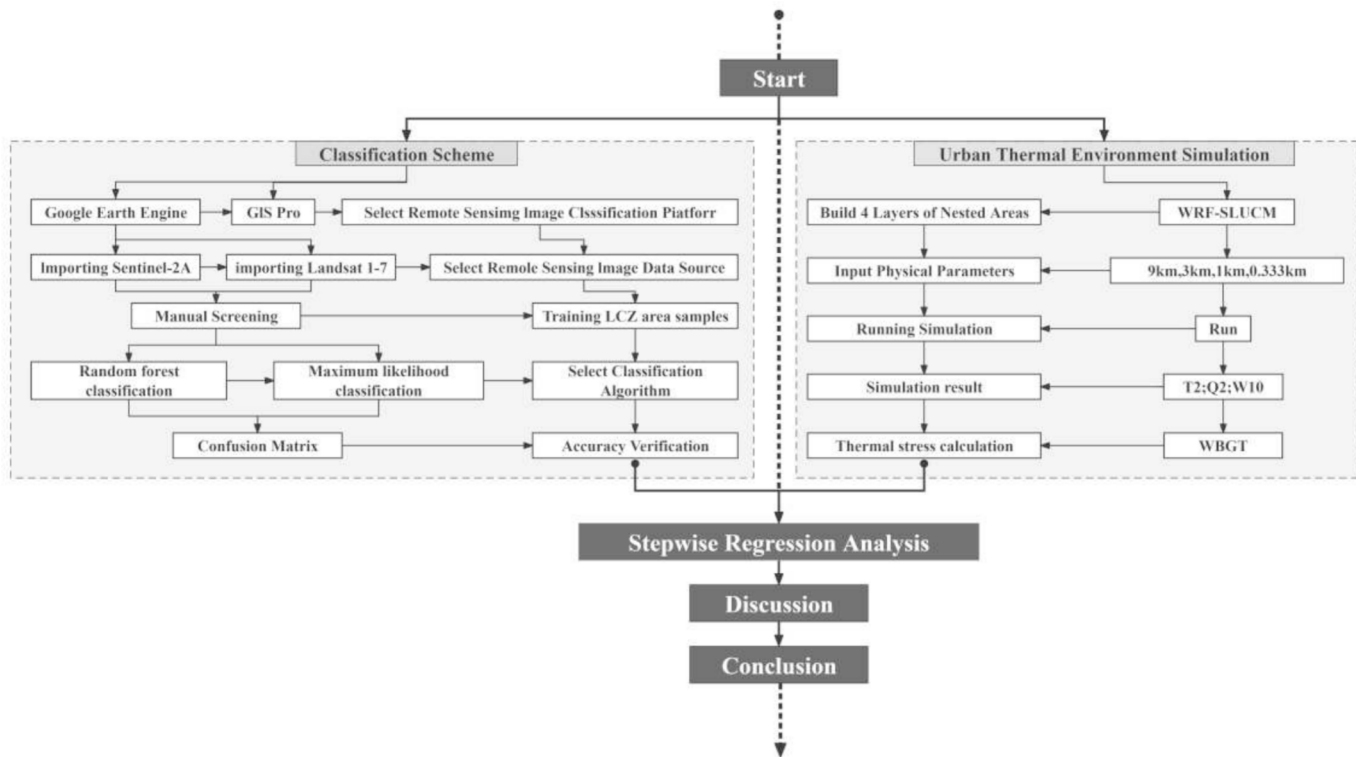


Fig. 1. Flowchart of the research process in this study.

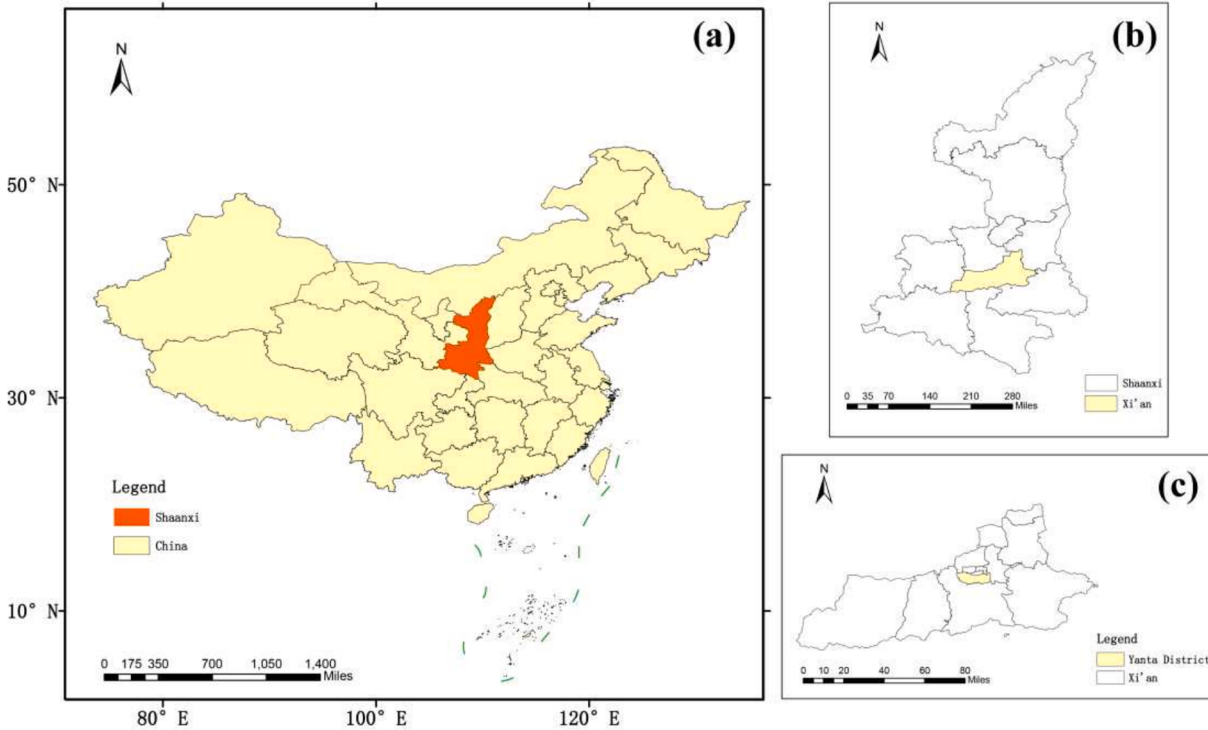


Fig. 2. Location of the study area in China.

2.2. Local climatic zone (LCZ) classification

The classification methods based on LCZ include manual sampling, remote sensing databases, and GIS-based methods (Weng, 2012; Bechtel et al., 2019; Bechtel et al., 2015). Among these methods, remote sensing

data have advantages such as convenient acquisition, low cost, and extensive coverage area. Supervised classification methods based on openly accessible remote sensing images are increasingly applied to LCZ classification. Scholars have further developed the World Urban Database and Access Portal Tools (WUDAPT) method, using remote sensing

Table 1

Remote sensing image information used in the study area.

position	Xi'an City, Shaanxi Province
Sensor type	Sentinel-2A/Landsat 1–7
Start time	2009-06-01 (2009 imagery) 2014-06-01 (2014 imagery) 2019-06-01 (2019 imagery) 2023-06-01 (2023 imagery)
End time	2009-06-30 (2009 imagery) 2014-06-30 (2014 imagery) 2019-06-30 (2019 imagery) 2023-06-30 (2023 imagery)
Cloud cover	0 ~ 10 %

technology to create supervised LCZ maps based on remote sensing images (Gao et al., 2020; Hay Chung et al., 2021; Gorelick et al., 2017; Ren et al., 2019). However, this approach brings significant computational and storage burdens to local computing platforms, including data acquisition and storage and parsing complex file formats, which may render many researchers and operational users unable to utilize these tools (Bechtel et al., 2019; Xu et al., 2018). Additionally, the current WUDAPT workflow based on random polygon sampling may lead to error propagation due to disproportionate sampling of specific LCZs (Li et al., 2022). In light of these challenges, this study plans to utilize Google Earth Engine, a cloud-based platform that provides easy access to high-performance computing resources for processing massive geospatial datasets without the current constraints associated with these resources (Xu et al., 2018).

The spatial resolution of remote sensing impacts classification accuracy significantly, and due to the clear advantage in spatial resolution of the Sentinel (10 m) series of remote sensing images, this study employs Sentinel-2A series remote sensing images. Stewart and Oke (2012) classified the urban structure of Bangalore, India, into seven categories using different resolution remote sensing images combined with the MLP deep learning classification method. They also extensively explored the impact of different resolution remote sensing data on classification accuracy, finding that overall accuracy increases with increasing spatial resolution (30 m, 10 m, 5 m) in urban and rural areas. In contrast, the 10 m resolution image (Sentinel-2A) performs better in transition areas.

The differentiation of 17 LCCS classes is mainly accomplished through several spectral indices, including NDVI (Normalized Difference Vegetation Index), NDWI (Normalized Difference Water Index), EVI (Enhanced Vegetation Index), BSI (Bare Soil Index), and IBI (Imperviousness Built-up Index). Meanwhile, height information and average daily/nightly band radiance values are added to the inputs for refining LCZ construction types. Urban digital elevation models (DEMs) provide more reasonable height-related classifications, demonstrating that additional height information to refine building classification can improve the accuracy of LCZ classification (Wang et al., 2023; Li et al., 2022). Hay's study (Gao et al., 2020) showed that there are elite variables with relatively higher contributions in LCZ classification using the RF classifier. The input of these elite variables ensures higher classification accuracy, and it was found that the average daily/nightly band radiance value (avg_rad) is the most crucial variable in LCZ classification. For specific classification feature information, (Table 2).

First, the ground observation data were processed using predefined Google Earth Engine (GEE) functions, including cloud removal and clipping to the study area. The next step involved selecting training areas from Google Earth satellite images on the GEE platform for each LCZ type (from LCZ-1 to LCZ-G). We selected 60–100 samples for each LCZ type for subsequent urban structure identification. To avoid errors, these samples covered the entire study area as evenly as possible. The selected samples were divided into a 70 % training set and a 30 % validation set, and then the Random Forest (RF) classification method was used for urban structure identification (Gao et al., 2020).

The Random Forest (RF) algorithm is an emerging machine learning

Table 2

Spectral index information used as input for LCZ classification process.

Spectral index	Formula
NDVI (Normalized vegetation index)	$NDVI = (\rho_{NIR} - \rho_{red}) / (\rho_{NIR} + \rho_{red})$
NDWI (Normalized water index)	$NDWI = (\rho_{Green} - \rho_{NIR}) / (\rho_{Green} + \rho_{NIR})$
EVI (Enhanced vegetation index)	$EVI = 2.5 \times \frac{\rho_{NIR} - \rho_{red}}{\rho_{NIR} + 6.0\rho_{red} - 7.5\rho_{Blue} + 1}$
BSI (Bare land index)	$BSI = \frac{((\rho_{NIR} + \rho_{red}) - 2\rho_{Green})}{((\rho_{NIR} + \rho_{red}) + 2\rho_{Green})}$
IBI (Urban construction index)	$IBI = \frac{\frac{2\rho_{SWIR1}}{\rho_{SWIR1} + \rho_{NIR}} - \left[\frac{\rho_{NIR}}{\rho_{NIR} + \rho_{red}} + \frac{\rho_{Green}}{\rho_{Green} + \rho_{SWIR1}} \right]}{\frac{2\rho_{SWIR1}}{\rho_{SWIR1} + \rho_{NIR}} + \left[\frac{\rho_{NIR}}{\rho_{NIR} + \rho_{red}} + \frac{\rho_{Green}}{\rho_{Green} + \rho_{SWIR1}} \right]}$
DEM (Digital elevation model)	/
Avg rad (Average daily/night band radiation value)	/

algorithm widely used in regression and classification tasks. It consists of multiple decision trees, where results are collected by randomly sampling from each decision tree and then aggregated through either majority voting or averaging to provide relatively stable and accurate results (Huang et al., 2017; Logan et al., 2020; Comber et al., 2012). Moreover, the RF algorithm can output the relative importance of each predictor variable, providing results in a ranked manner (Gwet, 2008).

Through the above steps, we obtained the urban structure of Xi'an City and further analyzed the dynamic changes in its urban structure. To verify the accuracy of the RF classifier for remote sensing image classification, we used a K-by-K matrix for validation (Skamarock et al., 2019), referred to as a confusion matrix or error matrix. This validation method is a standard method for accuracy assessment, and by calculating metrics such as the kappa coefficient and overall accuracy from the confusion matrix, we can determine whether the LCCS classification by RF aligns with reality.

Evaluation metrics include the producer's accuracy (PA), user's (UA), overall accuracy, and Kappa index. PA and UA are calculated using an equation and a confusion matrix. (1) and (2). N is the number of total samples, K is the number of categories classified, and the number of samples classified as i belong to j in the reference class. Where is the overall accuracy calculated by Eq. (3), is calculated by Eq. (5), and the overall accuracy and Kappa index (Li and Liu, 2021) are finally calculated. For LCZ map quality control, the overall accuracy and kappa coefficient must fall within the acceptable ranges proposed by Gorelick et al. (2017), which are 50 % and 0.5, respectively.

$$PA_j = \frac{N_{jj}}{N_{+j}} = \frac{N_{jj}}{\sum N_{ij} (j = 1 \sim k)} \quad (1)$$

$$UA_i = \frac{N_{ii}}{N_{i+}} = \frac{N_{ii}}{\sum N_{ij} (i = 1 \sim k)} \quad (2)$$

According to PA_j and UA_i , the overall accuracy and Kappa index (k) can be obtained from Eqs. (3) and (4):

$$OA = \frac{\sum N_{ii}}{n} (i = 1 \sim k) = \frac{\sum N_{jj}}{n} (j = 1 \sim k) \quad (3)$$

$$k = \frac{p_0 - p_e}{1 - p_e} \quad (4)$$

where p_0 is the overall accuracy calculated by Eq. (3), p_e is calculated by Eq. (5):

$$p_e = \frac{\sum (N_{i+} \times N_{+j})}{n \times n} \quad (5)$$

2.3. Mesoscale environmental simulation

In the simulation, only the main urban area of Xi'an city center was

selected to verify the climate environment associated with land use changes. The WRF model is a non-hydrostatic model that has been widely applied in various areas, such as weather forecasting, extreme weather and tropical cyclone simulations, as well as studies on land use and land cover changes (Ryu et al., 2016). However, previous models often failed to accurately represent the actual urban vegetation conditions, simplifying the urban evapotranspiration processes, which could significantly impact the results of urban climate simulations (Liu et al., 2017). Research by Giannaros et al. (2018) and Fang et al. (2019), among others, further emphasized the role of vegetation and tree evapotranspiration in the SLUCM (Single Layer Urban Canopy Model). Meanwhile, Liu et al. (2017) et al.'s study, which employed the WRF-SLUCM model, further clarified the spatiotemporal impacts of hydrological processes on urban microclimates. These studies have continuously improved the WRF-SLUCM model, demonstrating its enhanced reliability in urban climate simulations. The performance of the WRF model in the study area primarily relies on high-precision surface and urban canopy characteristic data to optimize parameter estimation. However, some of the higher-precision relevant data are often difficult to obtain or are missing, which can result in the exclusion of such data from the model setup. This may, to some extent, affect the simulation results, though generally, the model is considered to be stable (Parsons, 2006).

This study chose the WRF-SLUCM model as the simulation tool, with numerical simulations using version 4.3.1 of the Weather Research and Forecasting (WRF) model. The primary physical schemes used for model simulation are shown in Table 3. For this WRF-SLUCM simulation, we configured four nested domains, as shown in Fig. 3, labeled as D01, D02, D03, and D04, with horizontal grid spacing increasing from outer to inner domains: D01 (9 km), D02 (3 km), D03 (1 km), and D04 (0.333 km). The initial and boundary conditions for the atmospheric field were obtained from the Global Data Assimilation System (GDAS) of the National Centers for Environmental Prediction (NCEP) in the United States (<https://rda.ucar.edu/datasets/ds083.3/>).

To capture the thermal environment changes in the main urban area of Xi'an city center, we designed four numerical experiments: (1) LULC2009, using land cover data from 2009. (2) LULC2014, using land cover data from 2014. (3) LULC2019, using land cover data from 2019. (4) LULC2023, using land cover data from 2023. The meteorological data used in the four experiments consistently differentiate the changes from different land uses. Land use data are obtained from NASA ([https://LPDAAC-MCD12Q1\(usgs.gov\)](https://LPDAAC-MCD12Q1(usgs.gov))) and the National Tibetan Plateau Data Center (<https://data.tpdc.ac.cn>). June 21st was chosen as the simulation day because it is the summer solstice with the most extended daylight hours. The simulation time is from 08:00 local time on June 21st to 08:00 local time on June 22nd, totaling 24 h. Table 3 shows the input configurations for the Xi'an simulation.

2.4. Calculation of the heat stress index

To date, over 100 heat stress indices have been developed globally, with a limited number of indices being accepted as standard measures. One of the most renowned among them is the Wet Bulb Globe Temperature (WBGT) index, which was proposed by Yaglou and Mynard in 1957 and adopted as a standard measure in 1989 (Teimori et al., 2020; Ono and Tonouchi, 2014). This index has gained widespread application worldwide due to its simplicity, reliability, and ease of use (Cabral et al.,

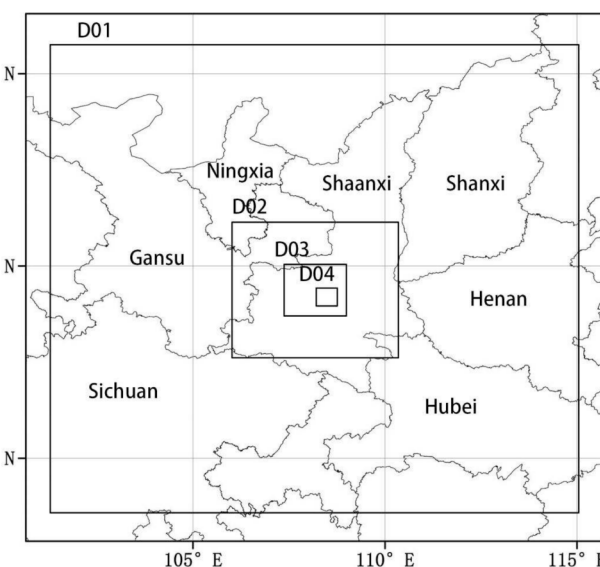


Fig. 3. Illustration of the four nested model domains used for WRF simulations.

2018). This study employs a simplified version of the WBGT calculation formula (Eq. (6)) (Cao et al., 2022), which takes the simulation results of WRF-SLUCM—air temperature, specific humidity, solar radiation intensity, and wind speed—as input parameters. By solving this equation, the WBGT calculation results are obtained, and upon verification, the average estimation error is approximately $\sim 0.11^{\circ}\text{C}$.

$$\begin{aligned} T_{\text{WBGT}} = & 0.735T_a + 0.0374RH + 0.00292 \times T_a \times RH + 7.619 \\ & \times 10^{-3}SR - 4.557 \times 10^{-3}SR^2 - 0.0572v - 0.4064 \end{aligned} \quad (6)$$

where, T_a : Temperature ($^{\circ}\text{C}$), RH: relative humidity (%), SR: sunshine amount (kW/m^2), v: wind speed (m/s).

2.5. Correlation analysis

We divided the study area into 15 sample regions for analysis. Seventeen LCZ types were used as the basic units for correlation analysis to investigate the relationship between different LCZs and urban thermal environments. Correlation heatmap were used to illustrate the correlation between each LCZ and heat stress. Subsequently, the data were normalized to prevent the dimensions of the data from affecting the analysis process, using the following formula (7):

$$Y_i = \frac{X_i - X_{\text{MIN}}}{X_{\text{MAX}} - X_{\text{MIN}}} \quad (7)$$

where X_i is the original value of the variable, X_{MIN} is the minimum value of the variable, and X_{MAX} is the maximum value of the variable. Y_i represents the normalized index.

Then, the Pearson correlation coefficient was used to measure the linear correlation between each LCZ type and various urban thermal environment indicators.

3. Results

3.1. LCZ classification results

The distribution of LCZs is illustrated in Figs. 4 and 5. Fig. 4a-d represent the 2009, 2014, 2019, and 2023 classification results, respectively. The area of built-up land types in Xi'an has rapidly increased from 2009 to 2023. The expansion trend is characterized by the rapid spread of the built-up land type LCZ4, particularly on the northern and southern sides of the city. Among natural land cover types,

Table 3
The WRF physical parameterizations.

Model version:	Version 4.3.1
Horizontal grid resolution of four domains:	9 km, 3 km, 1 km, 0.333 km
Land surface model:	NOAH
Radiation scheme:	RRTMG
LULC data:	USGS/TPDC
Microphysics scheme:	WSM-5

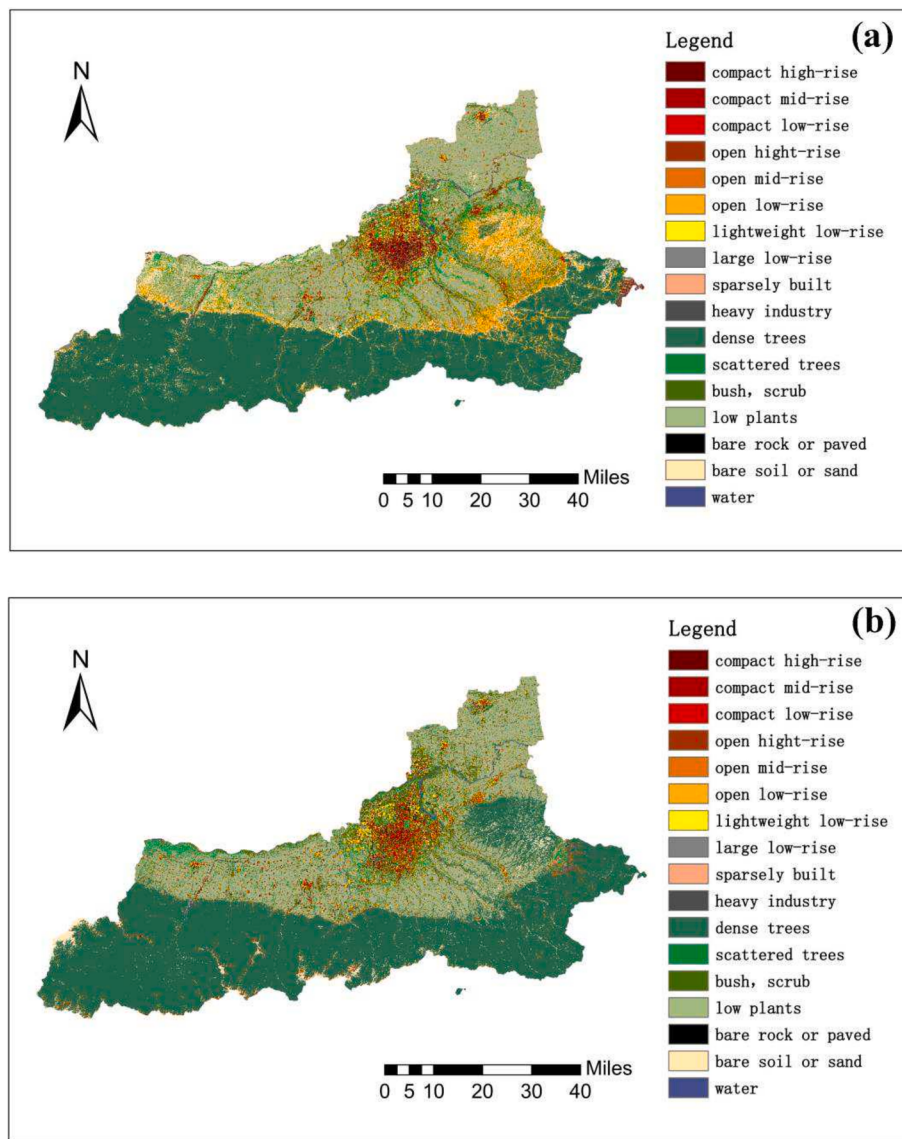


Fig. 4. Classification results of local climatic zones in Xi'an: (a) 2009; (b) 2014; (c) 2019; (d) 2023.

LCZA and LCB decreased by 4.85 % and 3.28 %, respectively. LCZA increased to 50.73 % in 2014, but then rapidly deteriorated to 32.97 % by 2019, before recovering to 40.24 % in 2023. LCZC, D, E, F, and G all showed varying degrees of increase, with LCZG experiencing a rise of 0.18 % from 2009 to 2023. This increase is noteworthy in an urban environment with limited water resources, and the growth of water bodies primarily occurred in the western and southern parts of the city. These developments reflect the local government's commitment to building a sustainable urban environment.

Figs. 6 and 7 display the areas of each LCZ within Xi'an City and Yanta District for different years. The area of built-up land types in Yanta District has also maintained a high growth rate, with dark-colored areas continually expanding outward from the center. This change reached its peak during the period from 2014 to 2019. The increase in dark-colored areas signifies the emergence of more high-rise residential buildings in the region, indicating that the area's urban structure is evolving towards greater height and density. As the city's core area, this development aligns with the rapid population and economic growth in Yanta District from 2009 to 2023. However, it is worth noting that the areas of LCZ1 and LCZ2 have remained almost unchanged, suggesting that the historically built residential buildings in the area have not undergone

significant alterations. Tables 4 and 5 show the percentages of each LCZ type within the entire area. Fig. 8 depicts the changes in each LCZ from 2009 to 2023.

From the central area of Xi'an to its surrounding suburbs, the pixel colors transition from deep red to lighter shades, indicating a gradual decrease in building density and height. Table 5 shows that in Xi'an, the Land Cover Types (LCZ) accounted for 16.67 % of the total area in 2009, decreasing to 9.80 % in 2014, and fluctuating to 15.86 % in 2019 and 13.62 % in 2023. Such significant changes stem from China's rapid urbanization process post-2008, during which the Chinese government implemented a series of effective urban development policies aimed at increasing urbanization rates, expanding urban areas, adjusting industrial layouts and structures, enhancing urban infrastructure, and reforming land and housing systems. The study area is located in the central district of Xi'an. Table 6 indicates that in Yanta District, the predominant LCZ types were LCZ7 and LCZ2 in 2009 and 2014, accounting for 11.97 % and 9.35 % respectively, while in 2019 and 2023, LCZ4 became the most prevalent type, representing 18.73 % and 22.02 % respectively. Fig. 8 illustrates the changes in LCZ areas in Xi'an and Yanta District from 2009 to 2023. The most significant change in Xi'an is observed in LCZD, which increased by 1,060,058,457 m² from 2009 to

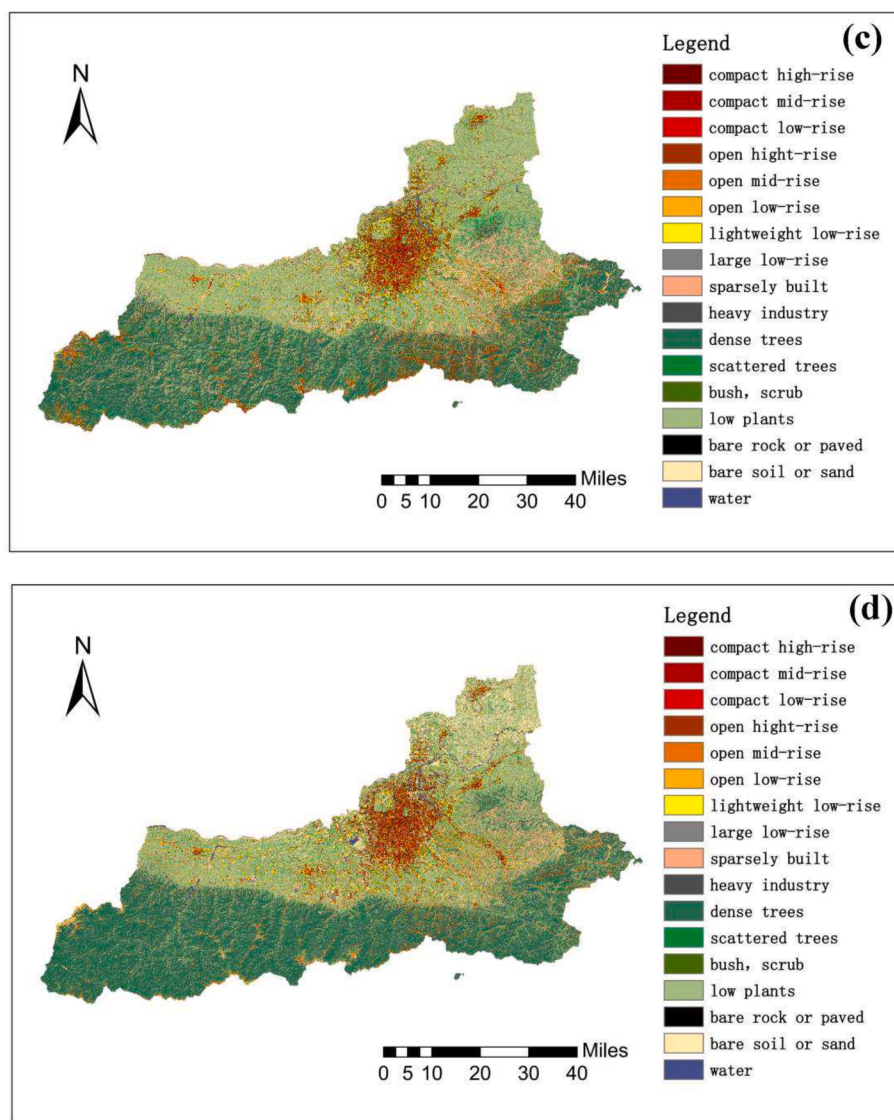


Fig. 4. (continued).

2023, followed by LCZ6, which decreased by 671,143,728 m². In Yanta District, the most notable change occurred in LCZ4, which increased by 28,675,307 m² over the past 14 years, while LCZB decreased by 23,872,260 m².

Tables 6–9 display the confusion matrices used for accuracy assessment for 2009, 2014, 2019, and 2023, respectively. We observed that the LCZ10 type consistently had the lowest accuracy in all classifications. It was frequently misclassified as LCZ8 in 2009 and 2014, LCZ1 in 2019, and LCZ8 and LCZ2 in 2023. After calculation, the Overall Accuracy was 73.80 %, 74.20 %, 68.32 %, and 69.20 %, respectively, and the Kappa index was 0.7139, 0.7204, 0.6441, and 0.6573, respectively. These values meet our accuracy requirements.

3.2. Simulated result

Within the study area, we selected two observation zones to collect actual data, and the values obtained from these zones were subjected to averaging processing. The Appendix Fig. 1 presents an error analysis comparing simulated values with actual observations. The overall error in temperature is generally insignificant. However, a significant error in humidity is observed between 15:00 and 1:00. As for wind speed, the overall error is not prominent, with notable deviations primarily occurring at 8:00 in the morning and 19:00 and 20:00 in the evening.

Air temperature, wind speed, specific humidity and WBGT reflect the climatic environment within the study area. Fig. 9 and Fig. 10 show the spatial distribution of four climate parameters in Yanta District in 2009, 2014, 2019 and 2023. The lowest temperature at 6:00 am is 23.21 °C, 23.09 °C, 22.90 °C and 22.78 °C, respectively. The highest temperatures were 26.90 °C, 26.77 °C, 26.69 °C and 26.29 °C respectively. The minimum humidity (g/kg) was 11.23, 11.29, 11.21, 11.42, respectively. The highest humidity (g/kg) was 12.59, 13.16, 12.23, 13.46, respectively. The lowest wind speed (m/s) were 0.12, 0.09, 0.10, 0.19, respectively. The maximum wind speed (m/s) were 6.03, 6.22, 6.23, 6.06, respectively. The lowest values of WBGT were 23.01 °C, 22.99 °C, 23.01 °C and 23.14 °C, respectively. The highest values were 24.98 °C, 25.19 °C, 24.94 °C and 25.36 °C. At 14:00, the temperature increased significantly, with the lowest temperature being 30.80 °C, 30.80 °C, 30.81 °C, 28.87 °C; The maximum temperature was 32.06 °C, 32.09 °C, 32.06 °C, 32.17 °C, respectively. The minimum humidity (g/kg) is 6.17, 6.16, 6.16, 6.17; The highest humidity (g/kg) was 7.31, 7.31, 7.32, 10.98; The lowest wind speed (m/s) was 0.43, 0.40, 0.39, 0.22. The maximum wind speeds were 1.88, 1.89, 1.88 and 2.15, respectively. The lowest values of WBGT were 25.06 °C, 25.05 °C, 25.05 °C, 25.00 °C. The highest values were 25.90 °C, 26.02 °C, 26.03 °C and 27.77 °C.

Fig. 11 shows the 24-h average temperature, wind speed, specific humidity and WBGT change trends of the four simulated years from

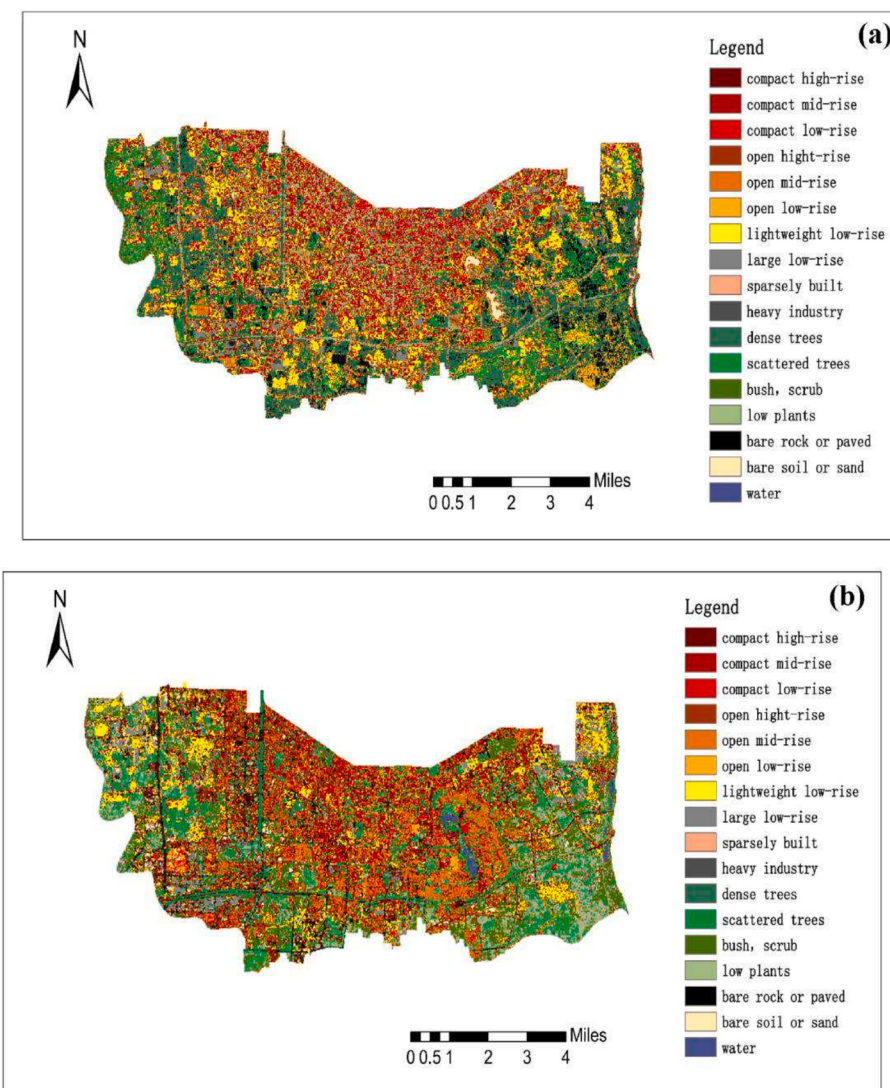


Fig. 5. Classification results of local climatic zones in Yanta District: (a) 2009; (b) 2014; (c) 2019; (d) 2023.

2009 to 2023. The most significant change in average temperature occurs at 19:00 PM from 2019 to 2023, with a decrease of 1.57°C . The most significant change in mean humidity occurred at 7:00 am from 2019 to 2023, with an increase of 0.87 (g/kg) . The most significant change in average wind speed occurred at 00:00 am in 2019–2023, with a decrease of 1.18 (m/s) ; The most significant change in average WBGT occurred at 00:00 AM in 2019–2023, with a decrease of 0.67°C .

Fig. 12 shows the hourly change values of four climate parameters throughout the day from 2009 to 2023. The overall temperature presents a downward trend, humidity an upward trend, wind speed a downward trend, and thermal stress a downward trend. The most significant temperature change occurred at 21:00 at night, with a drop of 1.48°C ; The most significant change in humidity occurred at 7:00 am, with an increase of 1.18 (g/kg) ; The most significant change in wind speed occurred at 19:00, with a decrease of 1.91 (m/s) ; The most significant change in WBGT occurred at 13:00 PM, with a drop of 0.7°C .

Fig. 13 shows the whole-day average of each climate parameter over four years. From 2009 to 2023, the whole-day average temperature in Yanta District decreased by 0.35°C ; the average humidity increased by 0.34 (g/kg) ; the average wind speed decreased by 0.36 (m/s) ; and the average WBGT decreased by 0.25°C .

3.3. Correlation analysis

We selected 15 regions of exactly the same area within the study area; therefore, We selected 60 different LCZ sample areas for correlation analysis. Table 10 shows the results of the Pearson correlation analysis, with ** indicating strong significance ($p < 0.01$) and * indicating moderate significance ($p < 0.05$); the results show that: (1) LCZ7, LCZ8, LCZ10, LCZA, LCZD, LCZE and LCZG, there were significant correlation between LCZF and WBGT (significant < 0.05); (2) There was significant positive correlation between LCZ7, LCZ8 and LCZ10, LCZE and WBGT, LCZA, LCZD, LCZG were significantly negatively correlated with WBGT.; (3) LCZ8, LCZ10, LCZA and LCZG had the most significant effect on WBGT, with correlation coefficients of 0.61 , 0.44 , -0.46 and -0.50 , respectively.

4. Discussion

4.1. Application of machine learning and remote sensing technology to urban structure classification

It has been demonstrated that the more detailed subdivision of urban structure using Local Climate Zones (LCZs) is feasible (Wang et al., 2021;

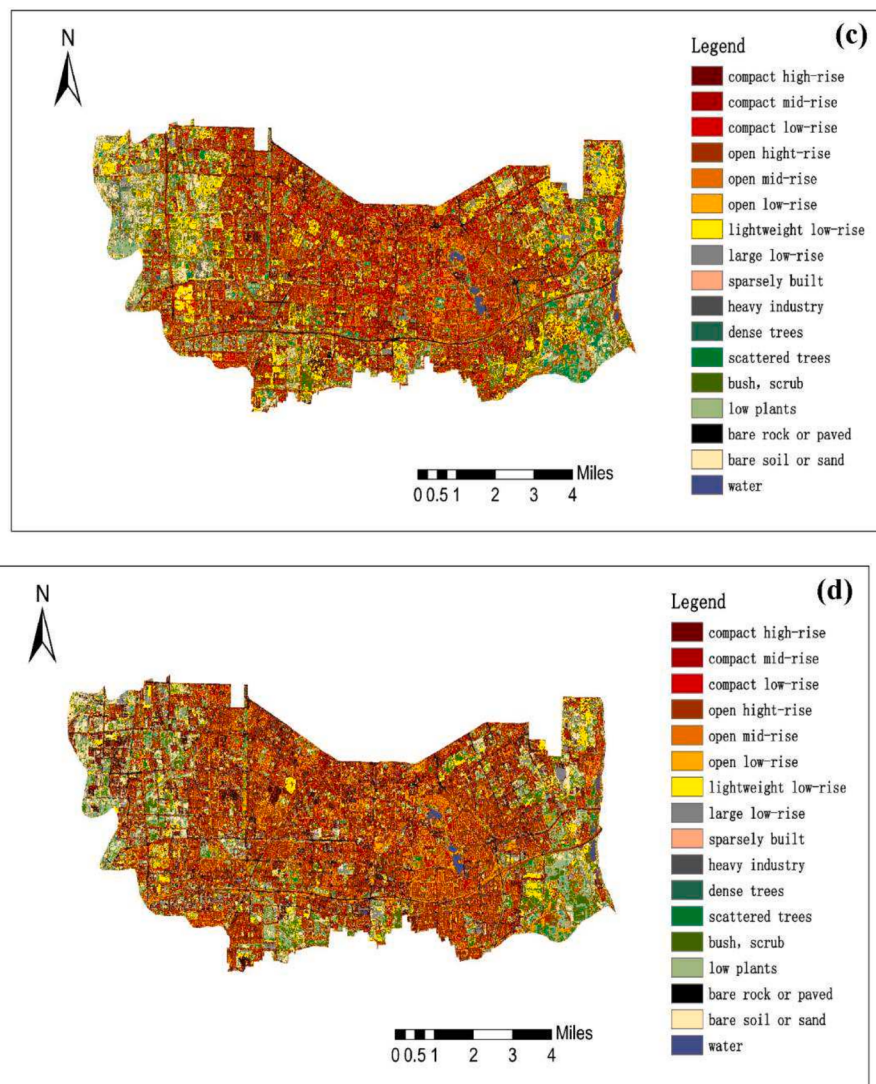


Fig. 5. (continued).

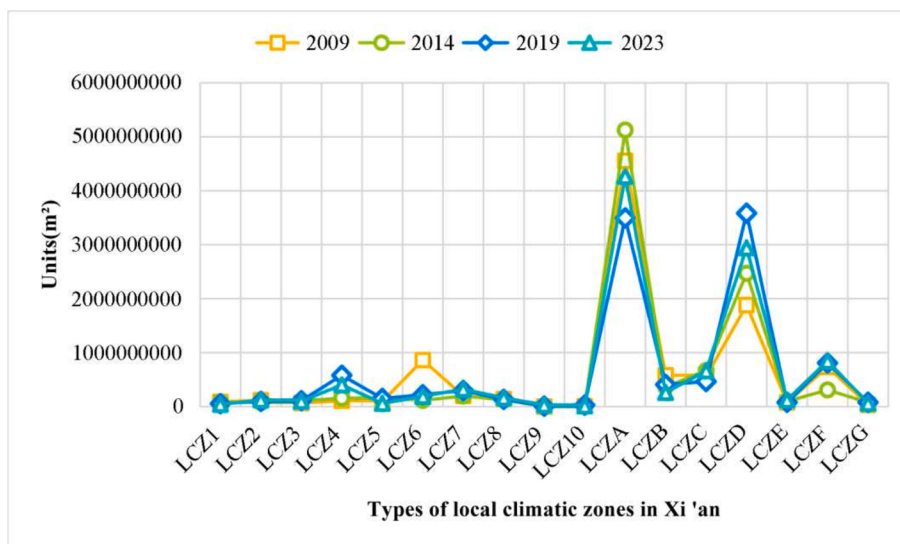


Fig. 6. Xi'an LCZ classification results.

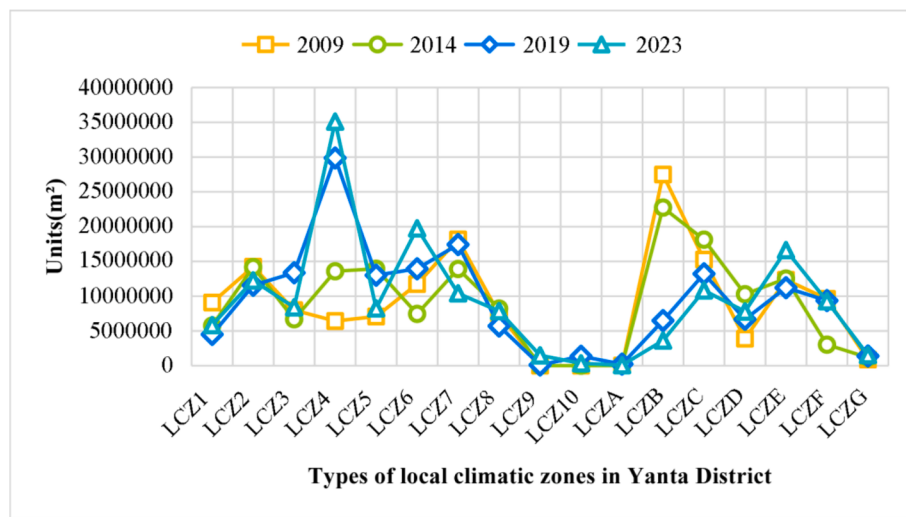


Fig. 7. LCZ classification results of Yanta district.

Table 4
LCZ classification results of Xi'an City in 2009, 2014, 2019 and 2023.

LCZ ID	Year 2009	Year 2014	Year 2019	Year 2023
LCZ 1	0.87 %	0.81 %	0.51 %	0.39 %
LCZ 2	1.19 %	0.75 %	0.92 %	1.15 %
LCZ 3	0.66 %	1.05 %	1.04 %	0.92 %
LCZ 4	1.07 %	1.57 %	5.47 %	3.81 %
LCZ 5	0.92 %	1.30 %	1.42 %	0.56 %
LCZ 6	8.53 %	1.14 %	2.07 %	1.80 %
LCZ 7	1.96 %	1.94 %	2.81 %	3.04 %
LCZ 8	1.39 %	1.24 %	1.27 %	1.53 %
LCZ 9	0.00 %	0.00 %	0.08 %	0.30 %
LCZ 10	0.08 %	0.00 %	0.27 %	0.12 %
LCZ A	45.09 %	50.73 %	32.97 %	40.24 %
LCZ B	5.74 %	3.60 %	3.85 %	2.46 %
LCZ C	5.52 %	6.62 %	4.39 %	6.25 %
LCZ D	18.62 %	24.46 %	33.80 %	27.74 %
LCZ E	0.76 %	0.97 %	0.75 %	1.16 %
LCZ F	7.28 %	3.06 %	7.62 %	7.96 %
LCZ G	0.32 %	0.75 %	0.75 %	0.59 %

Table 5
LCZ classification results of Yanta District in 2009, 2014, 2019 and 2023.

LCZ ID	Year 2009	Year 2014	Year 2019	Year 2023
LCZ 1	5.99 %	3.80 %	2.82 %	3.67 %
LCZ 2	9.38 %	9.35 %	7.25 %	7.69 %
LCZ 3	5.27 %	4.41 %	8.38 %	5.27 %
LCZ 4	4.24 %	8.95 %	18.73 %	22.02 %
LCZ 5	4.67 %	9.19 %	8.16 %	5.17 %
LCZ 6	7.74 %	4.91 %	8.74 %	12.39 %
LCZ 7	11.97 %	9.17 %	10.93 %	6.53 %
LCZ 8	4.90 %	5.42 %	3.58 %	4.93 %
LCZ 9	0.00 %	0.00 %	0.07 %	0.93 %
LCZ 10	0.00 %	0.00 %	0.85 %	0.21 %
LCZ A	0.01 %	0.03 %	0.15 %	0.05 %
LCZ B	18.12 %	14.99 %	4.07 %	2.27 %
LCZ C	10.06 %	11.95 %	8.29 %	6.79 %
LCZ D	2.56 %	6.78 %	4.18 %	4.89 %
LCZ E	8.14 %	8.26 %	7.03 %	10.43 %
LCZ F	6.34 %	2.00 %	5.88 %	5.82 %
LCZ G	0.58 %	0.77 %	0.88 %	0.96 %

Bechtel et al., 2015). Many studies have indicated that both the Random Forest method employed in this study on the Google Earth Engine (GEE) platform and the Maximum Likelihood Classification (MLC) method applied in GIS platforms are mature and feasible (Gao et al., 2020; Wang et al., 2023; Chowdhury, 2024). Furthermore, the use of confusion

matrices to validate the accuracy of classification results is a commonly used method (Wang et al., 2021; Gao et al., 2020; Wang et al., 2023; He et al., 2019; Cao et al., 2021). This study identified the urban structure of Xi'an and determined the land use and land cover in the study area. The classification results indicate that the proportion of LCZs representing building types in Xi'an was 16.67 % in 2009, 9.80 % in 2014, 15.86 % in 2019, and 13.62 % in 2023 for the entire area. Within the Yanta District of the study area, the proportions of LCZs representing building types were 54.16 %, 55.20 %, 69.51 %, and 68.81 %, respectively.

Additionally, based on the long-term classification results, we observed that changes in natural land cover types were most pronounced across Xi'an. Notably, LCZA saw a significant increase between 2009 and 2014, followed by a sharp decline from 2014 to 2019, before rebounding to levels close to those in 2009 by 2023. Such dramatic fluctuations may be attributed to the rapid urbanization process initiated by the Chinese government after the 2008 financial crisis. Starting in 2009, large-scale demolition of existing dense mid- and low-rise buildings occurred to pave the way for future modernization. However, from 2014 onward, China experienced substantial economic growth, with GDP maintaining high growth rates. Xi'an, as a rapidly emerging first-tier city, attracted a large amount of construction investment, leading to rapid urban expansion. The environmental challenges brought about by such rapid urbanization prompted the Chinese government to adopt sustainable development principles by 2020, fully committing to the construction of an ecological civilization. Various related policies and measures have contributed to the restoration of natural land cover types. The research results indicate that from 2009 to 2023, the area of land used for construction types in Xi'an has continuously expanded, while the area of dense natural vegetation has shown a declining trend. Similar conclusions were drawn by scholars such as He and Zhang, who argued that rapid urbanization is a common phenomenon in fast-growing developing countries (Lambin et al., 2001; Xu et al., 2019).

We also observed that the changes in construction types in Xi'an are mainly concentrated in LCZ4 and LCZ6, and their spatial distribution is predominantly focused in the northern and southern parts of the city. This can be attributed to the fact that since 2008, the real estate industry has become one of the main drivers of economic growth in China. The rapid population growth in Xi'an has also generated a substantial demand for housing. Meanwhile, as a historical city, Xi'an has been guided by a clear urban planning strategy from the Chinese government aimed at excavating and preserving its historical relics. The central area, with its long history, has been subject to limited development, while the large construction demand has been redirected mainly to the south and north,

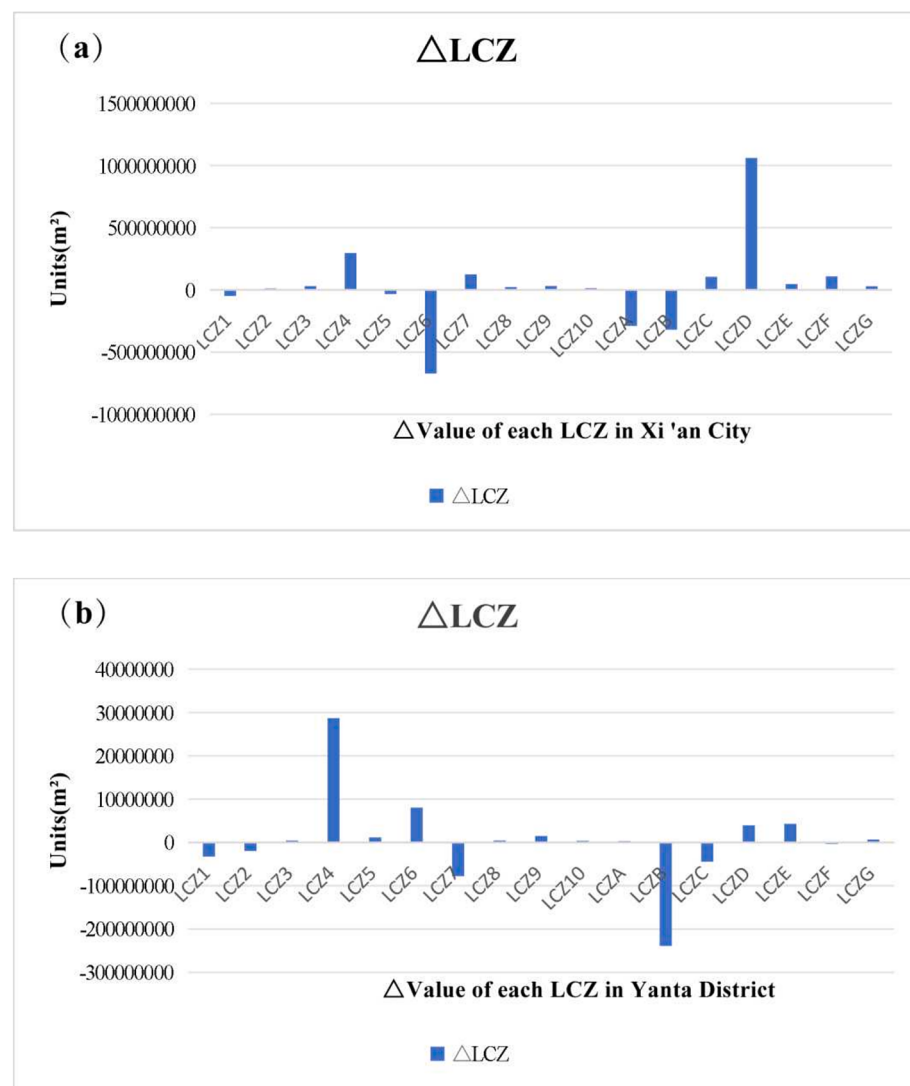


Fig. 8. Δ value of LCZ from 2009 to 2023: (a) LCZ Δ value of Xi 'an City; (b) LCZ Δ value in Yanta district.

Table 6

Confusion matrix of LCZ classification results for Xi'an in 2009.

LCZ ID	1	2	3	4	5	6	7	8	9	10	A	B	C	D	E	F	G	Total
1	7	3			1							1			1			13
2	1	23	2	5	1	3												35
3	1	1	15	3	1	1									1			23
4			1	47		3									3			56
5	1	1		1	8	2	1							2			2	17
6		3	3	2		60											1	70
7				1			12								3			17
8							12		1						1			15
9		1		1	1	2			18	1	1			1		1		28
10	2			1			1	5		6		71	1	2	2		1	16
A								2					15	1	2			78
B								1										19
C					1				1	1			2	13	1	2		22
D									1					17		2		20
E	2			2		2	2							1		13		22
F		1		2	1			1					1	1	1	14	1	24
G	1			1	1	1								2		18		25
Total	13	34	22	67	14	76	16	18	23	11	72	21	23	27	23	21	19	500
Overall Accuracy/%:	73.80														Kappa index:0.7139			

Table 7

Confusion matrix of LCZ classification results for Xi'an in 2014.

LCZ ID	1	2	3	4	5	6	7	8	9	10	A	B	C	D	E	F	G	Total	
1	9	3			1							1			1			15	
2	1	19	2	5	1	3												31	
3	1	1	15	3	1	1								1				23	
4				1	47									2		3		56	
5	1	1		1	8	2	1								2	1		17	
6		3	3	2		32									1			42	
7				1		1	12							3				17	
8								12				1				1		15	
9		1		1	1	2			18	1	1			1		1		28	
10				1			1	7		4						1		14	
A	1									2		71	1	2	2			79	
B						1							28	1	2			32	
C				1							1	1		2	13	1	2	22	
D									1						17		2	20	
E		1			2		2							1		23		29	
F			1	2	1			1		1				1	1	1	25	1	35
G	1				1	1	1							2			18	25	
Total	14	29	22	67	14	48	14	20	23	9	72	34	23	27	33	32	19	500	
Overall Accuracy/%:74.20																			
Kappa index:0.7204																			

Table 8

Confusion matrix of LCZ classification results for Xi'an in 2019.

LCZ ID	1	2	3	4	5	6	7	8	9	10	A	B	C	D	E	F	G	Total
1	14	3		4	1										3			26
2	1	16	2	4	1	3									3			30
3	1	1	15	3	4	1								1				26
4		1	107		3									2		3		116
5	1	3	5	3	60	2	1								2	1		24
6		3	3	2		6			1						1			70
7				1		1	12							3				17
8								12				1			1			15
9		1		1	1	2			18	1	1			1	1			28
10	2			1			1	4		4		11	1	2	2			13
A								2					7	1	2			18
B						1							2	5	1	2		11
C				1					1	1				17				14
D								1							17			20
E		2		8		2	2							1		13		28
F			1	2	1	1	1	1					2	2	1	10	1	24
G	1			1	1	1								2			18	25
Total	20	29	27	138	15	77	17	17	23	9	12	13	16	28	28	17	19	505
Overall Accuracy/%:0.6832																		
Kappa index:0.6441																		

Table 9

Confusion matrix of LCZ classification results for Xi'an in 2023.

LCZ ID	1	2	3	4	5	6	7	8	9	10	A	B	C	D	E	F	G	Total
1	11	3		2	1	1						1			2	1		22
2		17	2	2	3	2	1					2		1	2			32
3	1	3	11	5	3		1							2	1			27
4	2	5		108		3							2		1			121
5	1	2	4	2	12	6								3				30
6			1		4	48							1					54
7						12			1									14
8						1	13	1	1							2		18
9		2	1			1		10				1	1	3		1		20
10		2				1	2		3						1	1		10
A							1			13				2			1	17
B					4		4						7	2	1			18
C	1			1			1		2				2	11	1		5	24
D									2			2	1	23				29
E			2	2	2	2		1							19			28
F			1				2	2	1					5		15		26
G						1											22	23
Total	16	35	22	126	26	66	18	18	18	9	13	15	16	35	30	27	23	513
Overall Accuracy/%:69.20																		
Kappa index:0.6573																		

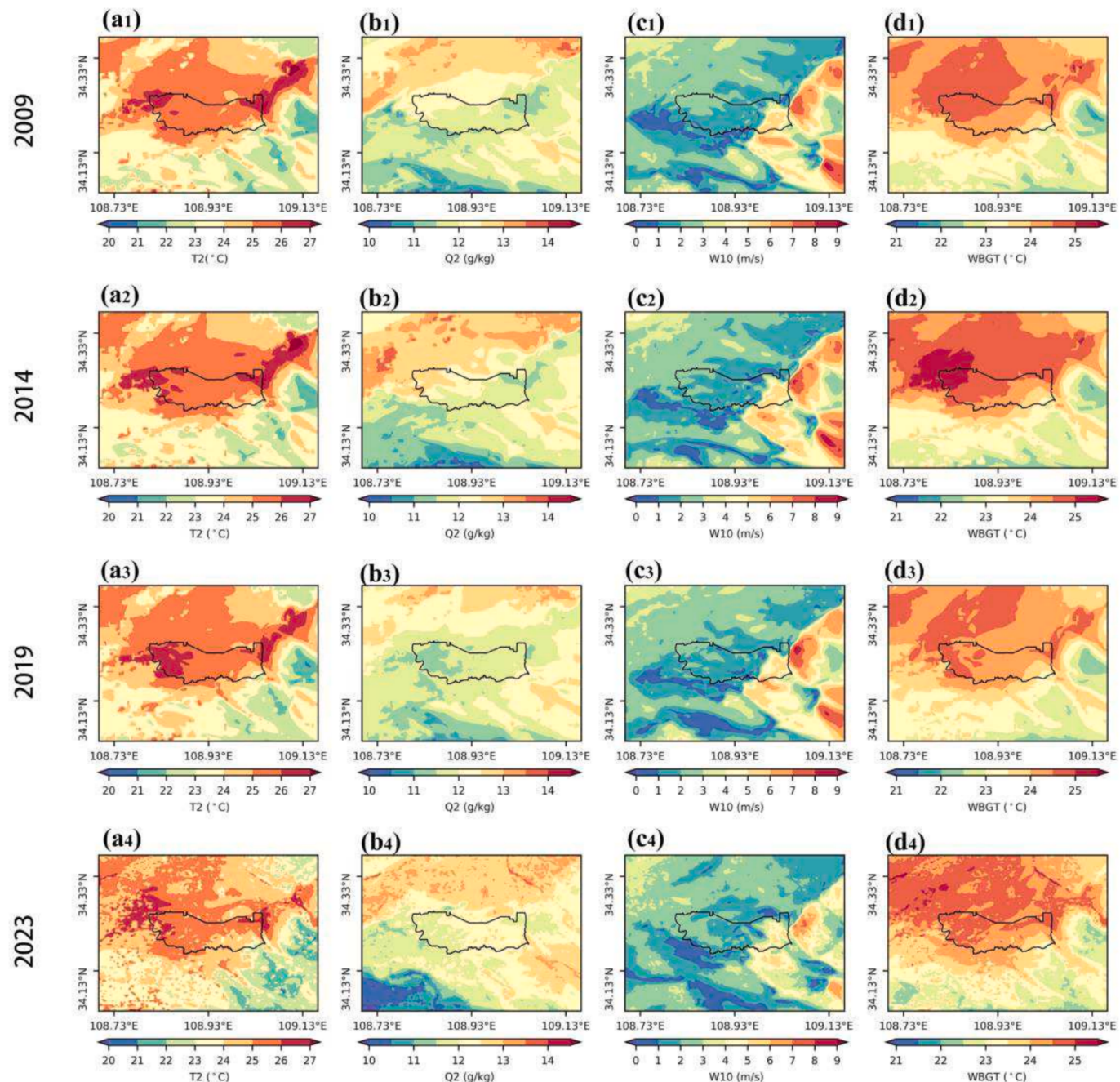


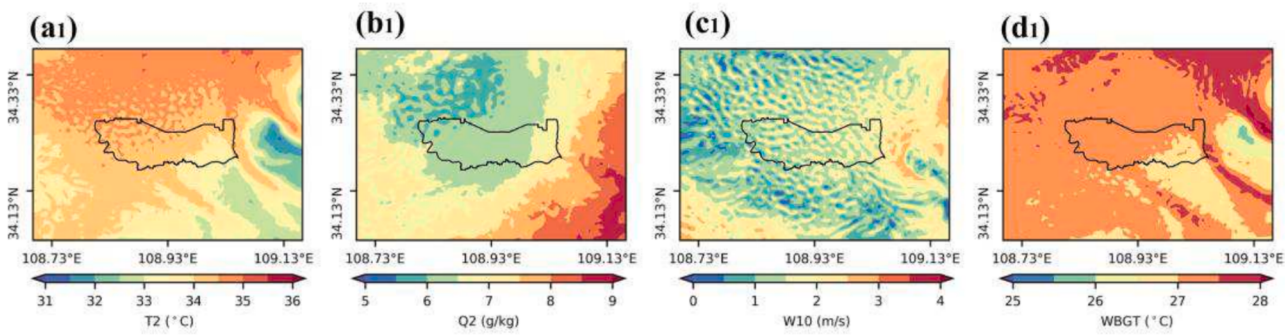
Fig. 9. Spatial distribution of temperature, humidity, wind speed and WBGT at 6:00 in Yanta District, 2009, 2014, 2019, 2023; (a1–a4) temperature; (b1–b4) humidity (c1–c4) wind speed; (d1–d4) WBGT.

resulting in the development of numerous medium-density high-rise residential areas. We believe that the same factors have led to the steady growth of LCZD and LCZF, with the exception of a brief decline in LCZF in 2014. This is because these two natural cover types are primarily concentrated in urban green spaces. With the expansion of the city, especially the residential areas, the corresponding increase in green spaces is not surprising.

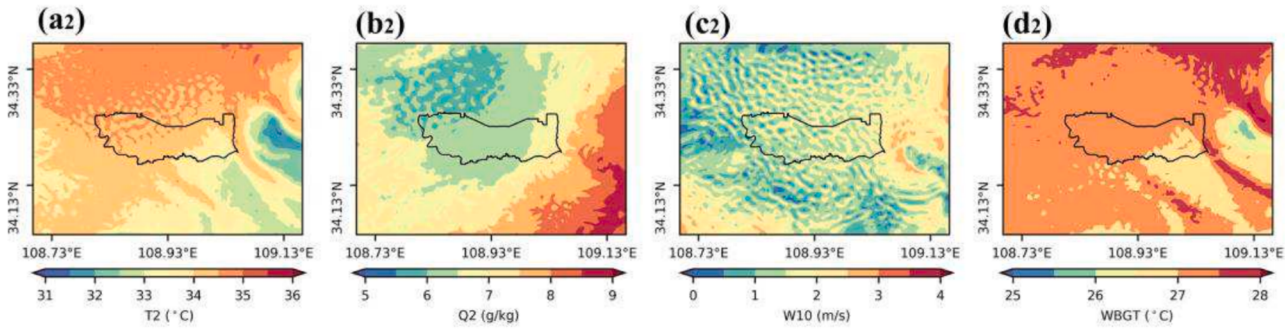
The Yanta area, as the economic core of Xi'an, experienced a rapid increase in construction type areas during the period from 2014 to 2019, growing by 14.31 %. This is an astonishing result, but it fully aligns with the reasons mentioned earlier. Among the construction types, LCZ4, LCZ6, LCZ7, LCZB, as well as LCZD and LCZE, all saw significant changes. The change in LCZ4 was consistent with the overall trend in Xi'an, but LCZ6 showed a marked increase. This is due to the economic

advantages of the area, which have concentrated a large number of affluent neighborhoods. On the other hand, the decline in LCZ7 and LCZB can be attributed to the demolition and redevelopment of the original urban villages, as well as the overconcentration of population. It is worth noting that the growth of LCZE and LCZD is also driven by economic factors and population concentration. The former led to the development of numerous large commercial plazas, while the latter resulted in the deterioration of both transportation and living environments. In response to these challenges, the government was forced to build extensive transportation and green infrastructure. From 2009 to 2023, the proportion of open high-rise, open mid-rise, and dispersed buildings in Yanta District continued to increase, while the proportion of compact high-rise, compact mid-rise, single-layer dense buildings, and heavy industrial buildings continued to decrease. This indicates a trend

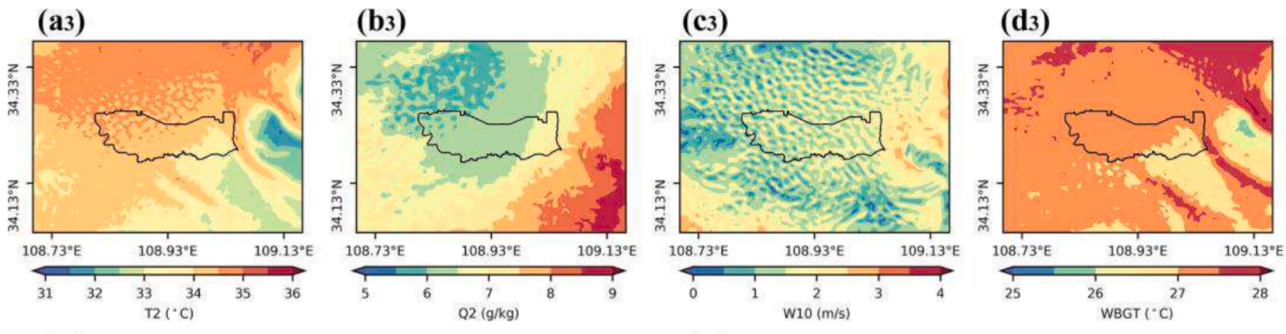
2009



2014



2019



2023

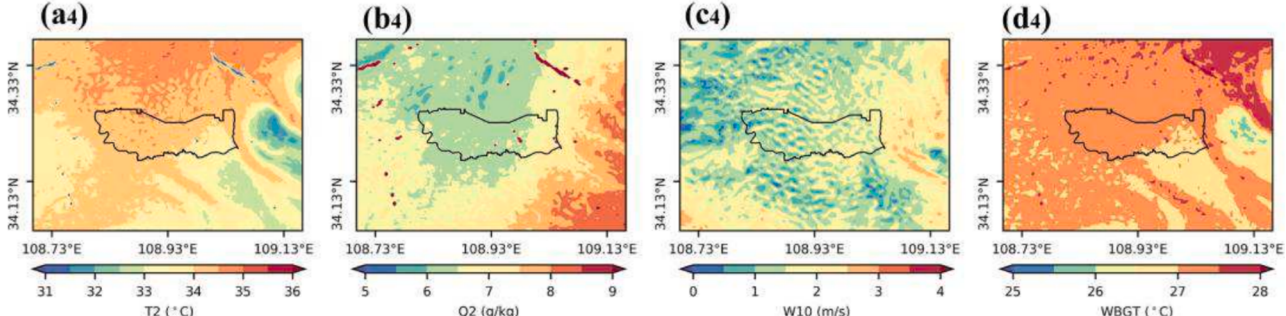


Fig. 10. Spatial distribution of temperature, humidity, wind speed and WBGT at 14:00 in Yanta District, 2009, 2014, 2019, 2023; (a1–a4) temperature; (b1–b4) humidity; (c1–c4) wind speed; (d1–d4) WBGT.

in urban construction in the central area of Xi'an towards higher heights and lower densities. At the same time, the thermal stress in the central area of Xi'an has been declining, indicating that high-rise buildings combined with lower densities contribute to improving the comfort and safety of the urban thermal environment (Wang et al., 2021; Peng et al., 2024; Das et al., 2022). The urban structure has a significant impact on urban thermal stress.

4.2. Overview of the influence of land cover on thermal environment in Yanta District

From a spatiotemporal distribution perspective, the thermal environment in the Yanta District from 2009 to 2023 has shown little change, with temperature, humidity, wind speed, and the shape of

thermal comfort zones remaining relatively stable. Combining LCZ classification maps and thermal environment distribution maps, it is observed that temperatures are higher, humidity and wind speeds are lower, and WBGT values are higher in the western and northern parts of the Yanta District. In contrast, significant improvements are noted in the eastern and southeastern regions. These areas are predominantly covered by vegetation, demonstrating the significant role of natural vegetation in improving the urban thermal environment (Demuzere et al., 2019; Sun et al., 2020; Issakhov and Abylkassymova, 2024; Yang, 2024).

Figs. 9–11 indicate that the changes in the thermal environment in the Yanta District primarily focus on humidity and wind speed, while temperature and the final calculated index, WBGT (Wet Bulb Globe Temperature), exhibit relatively stable changes. The peak change in

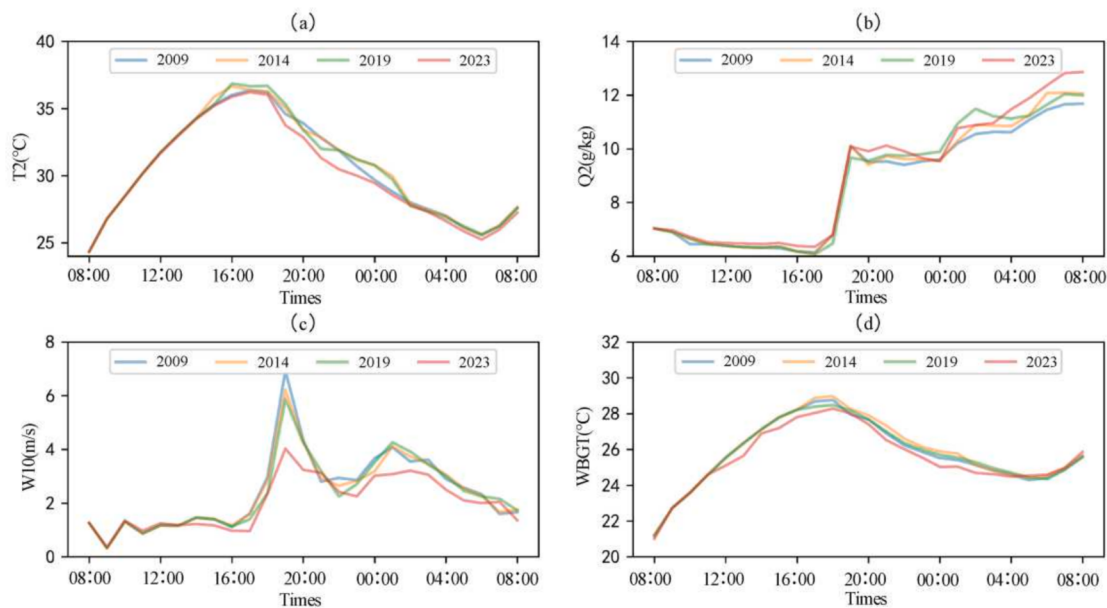


Fig. 11. 24-h mean temperature, wind speed, specific humidity and WBGT trends of four simulated days in Yanta District in 2009, 2014, 2019 and 2023.

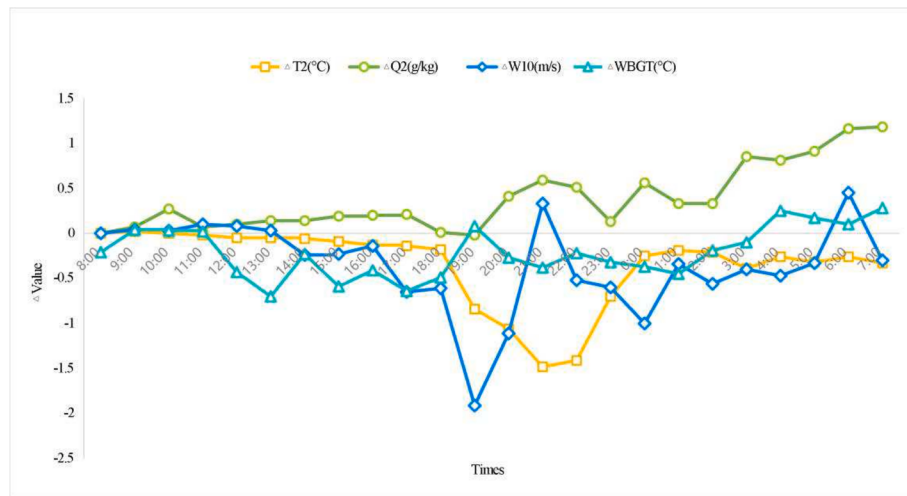


Fig. 12. The Δ values of temperature, specific humidity, wind speed and WBGT of 4 climate parameters in Yanta District during 2009–2023.

average humidity occurred at 7:00 AM from 2019 to 2023, increasing by 0.87 (g/kg). The most significant change in average wind speed occurred at 12:00 AM during the same period, with a decrease of 1.18 (m/s). The change in humidity may be attributed to the restoration of most natural cover types during this period, while the change in wind speed is likely due to the significant increase in LCZ4 and LCZ6 types, with the expansion of residential areas increasing the roughness of the urban surface. In particular, the clustering of high-rise residential buildings has rapidly degraded the local wind environment. Zhang et al. (2022)'s related study in Singapore reached similar conclusions, namely that the increase in building density leads to a significant reduction in wind speed, and they advocate for limiting regional density development.

The transformation of urban structural types may influence the flow and conversion of urban energy. The expansion of residential land often coincides with an increase in energy consumption, such as electricity and gas. These areas, characterized by a higher density of buildings, exhibit strong solar radiation absorption and reflection, as well as impeded long-wave radiation emission during the night, typically leading to the formation of localized urban heat islands (Issakhov and

Abylkassymova, 2024). Conversely, the increase in large areas of green spaces and water bodies helps improve the thermodynamic properties of the urban underlying surface. It facilitates air cooling and circulatory flow, thus isolating and limiting the spread of heat islands. This may ameliorate the urban microclimate and reduce the reliance on energy-consuming devices such as air conditioners (Yang, 2024). The reduction in wind speed weakens the airflow between urban and suburban areas and may also impact heat exchange processes within the city, such as the heat exchange between buildings and the air (Jie et al., 2023), which hinders the dissipation of heat within the urban interior. Decreased wind speed can further affect the pressure distribution within the city, leading to an increase in urban humidity and a more intense feeling of stuffiness. This increase in humidity alters the energy balance within the city. Water vapor in the air can store energy and release or absorb heat in the form of latent heat. Additionally, increased humidity may promote cloud formation and precipitation processes, which in turn influence the city's energy conversion through mechanisms such as reflecting solar radiation and absorbing or releasing latent heat (Ngarambe et al., 2021).

It is worth noting that all the peak changes were observed during the

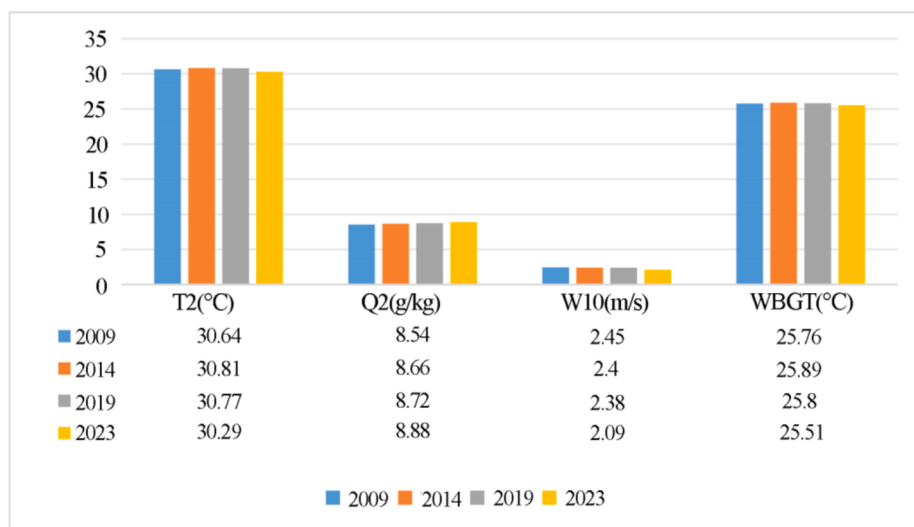


Fig. 13. Average temperature of Yanta District in 2009, 2014, 2019, 2023; Average temperature; Average humidity; Average wind speed; Average WBGT.

Table 10

Results of Pearson correlation analysis between different LCZ types and urban heat environment indicators.

	LCZ1	LCZ2	LCZ3	LCZ4	LCZ5	LCZ6	LCZ7	LCZ8
T2	*0.41	*0.30	0.17	-0.08	0.18	*-0.26	0.23	*0.28
Q2	-0.23	**-0.50	-0.1	0.04	*-0.32	0.11	-0.03	-0.09
W10	-0.18	-0.15	-0.1	-0.17	-0.05	0.07	0.02	*-0.28
WBGT	0.23	0.15	0.17	0.07	0.01	-0.2	*0.27	0.61**
	-0.6	-0.5	-0.4	-0.3	-0.2	0.2	0.3	0.4

	LCZ9	LCZ10	LCZA	LCZB	LCZC	LCZD	LCZE	LCZF	LCZG
T2	*-0.28	0.16	**-0.43	-0.04	-0.19	**-0.38	0.19	-0.19	**-0.37
Q2	0.22	-0.03	**0.39	0.02	*0.26	**0.44	-0.17	0.25	*0.30
W10	-0.17	-0.19	**0.35	*0.26	0.25	*0.26	*-0.30	0.04	**0.43
WBGT	0.08	**0.44	**-0.46	-0.24	-0.2	*-0.27	*0.30	0.05	**-0.50
	-0.6	-0.5	-0.4	-0.3	-0.2	0.2	0.3	0.4	0.6

^aThe numbers in the bottom row represent the color mapping of the correlation coefficients.

2019–2023 period, and the increase in some land cover types does not appear to show a simple linear relationship with thermal environment changes. For instance, the increase in LCZ4 during this period was less than that from 2014 to 2019, but its impact on the thermal environment exceeded that of the earlier period. This suggests a more complex, nonlinear relationship between changes in LCZ type area and thermal environment impact. Moreover, the thermal environment changes within the region may also be influenced by broader urban structural changes in surrounding areas, which warrants further investigation by other researchers.

Fig. 12 shows the overall trend of thermal environment changes from 2009 to 2023. In general, wind speed remains the parameter with the greatest variability, exhibiting a downward trend. However, the overall change in the Wet Bulb Globe Temperature (WBGT) is not very

pronounced, and there was even a significant decrease between 18:00 and 00:00. This suggests that over the past 15 years, the thermal environment of the study area has not deteriorated with rapid urban expansion, further indicating that the urban planning strategies of the Xi'an municipal government are both rational and effective. Deng et al. (2023)'s related study in 2023 found that the strongest urban development trend in Wuhan is also characterized by high-rise, medium-density intensification. They discovered that urban thermal stress in Wuhan increased by as much as 1.7 °C between 2008 and 2018, and confirmed the effectiveness of medium-density development in addressing environmental issues.

There is a clear connection between urban structure and the urban thermal environment (Jamei et al., 2019). In the study area, LCZ7, LCZ8, LCZ10, and LCZE are significantly positively correlated with urban

thermal stress, with correlation coefficients of 0.27, 0.61, 0.44, and 0.30, respectively. Large-scale, dense low-rise buildings, extensive low-rise structures, heavy industrial buildings, and extensive paving typically have more impervious surfaces and minimal vegetation cover, suggesting that a higher proportion of impervious surfaces enhances the urban heat island effect (Du et al., 2020; Simwanda et al., 2019). Additionally, LCZ1 and LCZ2 show significant positive correlations with temperature, and LCZ2 also shows a significant negative correlation with humidity, indicating that compact high-rise and mid-rise buildings are similarly detrimental to improving the urban thermal environment.

Correlation analysis results indicate that LCZA, LCZD, and LCZG are significantly negatively correlated with urban thermal stress, with correlation coefficients of -0.46, -0.27, and -0.50, respectively. These land cover types generally have more natural surfaces, further demonstrating the regulatory role of natural land surfaces in the urban thermal environment (Wang et al., 2023; Tan et al., 2024; Wu et al., 2022). From an urban structural perspective, to prevent the gradual intensification of the urban heat island effect and to improve the urban thermal environment, future urban planning should favor building types with lower proportions of impervious surfaces. This can be achieved by increasing building heights and reducing densities in urban planning metrics, thereby minimizing impacts on urban development while enhancing the urban thermal environment. Moreover, research indicates that LCZA and LCZG offer more pronounced benefits for WBGT improvement compared to other negatively correlated factors, suggesting that concentrated large areas of permeable surfaces are more advantageous than dispersed smaller areas. Thus, avoiding building clusters and leaving space between them to create low-density building clusters can help improve the urban thermal environment (Wu et al., 2022). Additionally, aggregated urban forests demonstrate better cooling effects than dispersed small patches of vegetation, highlighting the importance of strengthening urban green space construction as a crucial strategy (Menteş et al., 2024; Shi et al., 2023). Urban planning departments should strengthen the optimization of urban structure, emphasize urban environmental planning and renovation projects, and control the excessive expansion of urban construction land. Green transformations should be carried out for unreasonable building types, with the selective demolition of the most detrimental construction types. Additionally, the greening coverage in the region should be increased. The trend of high-rise, medium-density urban development should be maintained, but at the same time, the negative impacts on wind environments caused by the concentration of high-rise residential areas should be avoided. For example, this can be mitigated by creating regional ventilation corridors.

4.3. Limitations of the current research

Our research identified shortcomings in the LCZ classification system, particularly in the overlapping nature between construction types. For example, compact mid-rise buildings may be encompassed within compact low-rise buildings, and the distinction between compact high-rise and open high-rise buildings is minimal. Additionally, due to the lack of meteorological stations within the study area, verifying the accuracy of the mesoscale climate simulations using the WRF-SLUCM model with actual measurement data proves challenging. Previous studies have demonstrated that the WRF-SLUCM model is a reliable mesoscale simulation method and has been validated with observational data (Deng et al., 2023; Vinayak et al., 2022; Du et al., 2024). We plan to verify the accuracy of the WRF-SLUCM model in future research. Moreover, we have noted recent studies indicating that incorporating gridded urban canopy parameters into the WRF-SLUCM can enhance the model performance in urban areas (Deng et al., 2023; Zhang et al., 2020), and we intend to explore this approach in future research.

The scale and methodology of this study are limited to the scope of Xi'an City and may, therefore, not be universally applicable on a rural

(Ma et al., 2021); national or global scale. We encourage further in-depth research by other scholars to expand our understanding of this topic.

5. Conclusion

This study further validates the applicability of the LCZ classification system in urban structure classification. Utilizing the Google Earth Engine (GEE) platform and remote sensing tools, more advanced and mature classification methods, namely Random Forest and Maximum Likelihood Classification (MLC), were employed to identify the urban structure of Xi'an City and the Yanta District. Mesoscale climate simulations were conducted using the Weather Research and Forecasting with a Single-Layer Urban Canopy Model (WRF-SLUCM), and Wet-Bulb Globe Temperature (WBGT) was used to indicate urban heat stress. The relationship between urban structure and urban heat stress was confirmed through Pearson correlation analysis.

Accuracy validation demonstrated that the above classification methods can accurately identify each LCZ. The results indicate that urban structure has a significant impact on urban heat stress, with LCZA, LCZD, and LCZG showing noticeable improvements in the urban thermal environment. From 2009 to 2023, urban development in the study area exhibited a trend of increased building height and decreased density, resulting in a decrease in average daily temperature by 0.35 °C, an increase in average humidity by 0.34 g/kg, a decrease in average wind speed by 0.36 m/s, and a decrease in average WBGT by 0.25 °C. Employing lower-density building types and increasing large-scale urban forests in urban development can enhance the comfort and safety of the urban thermal environment.

Nevertheless, this study aims to provide a more accurate, simple, and reliable method for the long-term identification of urban structures, integrating this approach with urban heat environment research to ultimately develop a new method for long-term tracking and analysis. Simultaneously, from the perspective of the long-term development of future cities, research on the correlation between urban structure and the thermal environment in their long-term variations may provide guidance for future urban planning and urban construction. However, the study also has its limitations. Specifically, it lacks a more scientifically robust classification system for urban structures. The local climate zone (LCZ) classification system still has deficiencies in terms of definitional precision, and the high-precision mapping methods for LCZs discussed in this study are currently limited to urban areas. A key challenge for future research will be how to apply such methods at larger spatial scales, as well as how to develop a more advanced urban structure identification system.

CRediT authorship contribution statement

Kaipeng Huo: Writing – review & editing, Writing – original draft, Visualization, Software, Methodology. **Rui Qin:** Visualization, Data curation. **Jingyuan Zhao:** Funding acquisition, Conceptualization. **Xuan Ma:** Methodology, Investigation, Funding acquisition.

Declaration of competing interest

The authors declare that they have no known competing financial interests or personal relationships that could have appeared to influence the work reported in this paper.

Acknowledgments

This study was supported by the Xi'an Association for Science and Technology Youth Talent Promotion Project (959202313093), National Natural Science Foundation of China (52278087) and Beilin District Science and Technology Project (GX2454).

Appendix A

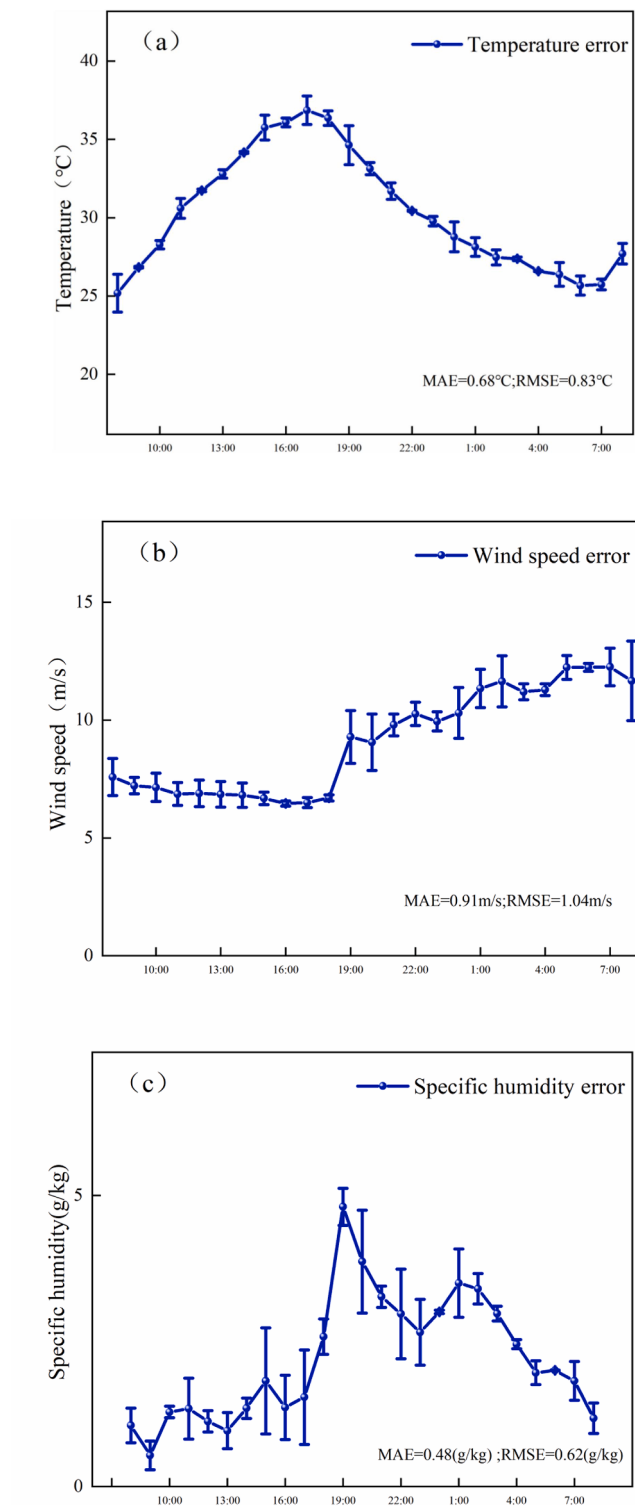


Fig. A1. Hourly comparison of WRF-simulated and actually observed temperatures (a), wind speeds (b), and humidity (c) during the analysis period (from 8:00 on June 21st, 2023, to 8:00 on June 22nd, 2023).

Data availability

The authors do not have permission to share data.

References

- Ali-Toudert, F., Mayer, H., 2006. Numerical study on the effects of aspect ratio and orientation of an urban street canyon on outdoor thermal comfort in hot and dry climate. *Build. Environ.* 41, 94–108.
- Arnfield, A.J., 2003. Two decades of urban climate research: a review of turbulence, exchanges of energy and water, and the urban heat island. *Int. J. Climatol.* 23, 1–26.
- Awuah, K.T., et al., 2018. Spatial resolution and landscape structure along an urban-rural gradient: do they relate to remote sensing classification accuracy? – A case study in the megacity of Bengaluru, India. *Remote Sens. Appl.: Soc. Environ.* 12, 89–98.
- Basara, J.B., Basara, H.G., Illston, B.G., Crawford, K.C., 2010. The impact of the urban heat island during an intense heat wave in Oklahoma City. *Adv. Meteorol.* 2010, 230365.
- Bechtel, B., et al., 2015. Mapping local climate zones for a worldwide database of the form and function of cities. *ISPRS Int. J. Geo Inf.* <https://doi.org/10.3390/ijgi4010199>.
- Bechtel, B., et al., 2019. Generating WUDAPT Level 0 data – current status of production and evaluation. *Urban Clim.* 27, 24–45.
- Blocken, B., Janssen, W.D., van Hooff, T., 2012. CFD simulation for pedestrian wind comfort and wind safety in urban areas: General decision framework and case study for the Eindhoven University campus. *Environ. Model. Softw.* 30, 15–34.
- Breiman, L., 2001. Random forests. *Mach. Learn.* 45, 5–32.
- Cabral, A.I.R., Silva, S., Silva, P.C., Vanneschi, L., Vasconcelos, M.J., 2018. Burned area estimations derived from Landsat ETM+ and OLI data: comparing genetic programming with maximum likelihood and classification and regression trees. *ISPRS J. Photogramm. Remote Sens.* 142, 94–105.
- Cao, Q., et al., 2022. Modeling intra-urban differences in thermal environments and heat stress based on local climate zones in central Wuhan. *Build. Environ.* 225, 109625.
- Cao, Q., Luan, Q., Liu, Y., Wang, R., 2021. The effects of 2D and 3D building morphology on urban environments: a multi-scale analysis in the Beijing metropolitan region. *Build. Environ.* 192, 107635.
- Chen, Y., Yang, J., Yang, R., Xiao, X., Xia, J., 2022. Contribution of urban functional zones to the spatial distribution of urban thermal environment. *Build. Environ.* 216, 109000.
- Chowdhury, M.S., 2024. Comparison of accuracy and reliability of random forest, support vector machine, artificial neural network and maximum likelihood method in land use/cover classification of urban setting. *Environ. Challenges* 14, 100800.
- Comber, A., Fisher, P., Brunsdon, C., Khmag, A., 2012. Spatial analysis of remote sensing image classification accuracy. *Remote Sens. Environ.* 127, 237–246.
- Das, M., Das, A., Momin, S., 2022. Quantifying the cooling effect of urban green space: a case from urban parks in a tropical mega metropolitan area (India). *Sustain. Cities Soc.* 87, 104062.
- Demuzere, M., Bechtel, B., Mills, G., 2019. Global transferability of local climate zone models. *Urban Clim.* 27, 46–63.
- Deng, X., et al., 2023. Characterizing urban densification and quantifying its effects on urban thermal environments and human thermal comfort. *Landsc. Urban Plan.* 237, 104803.
- Du, R., Liu, C.-H., Li, X.-X., 2024. A new method for detecting urban morphology effects on urban-scale air temperature and building energy consumption under mesoscale meteorological conditions. *Urban Clim.* 53, 101775.
- Du, J., Xiang, X., Zhao, B., Zhou, H., 2020. Impact of urban expansion on land surface temperature in Fuzhou, China using Landsat imagery. *Sustain. Cities Soc.* 61, 102346.
- Dymond, J.R., Bégué, A., Loseen, D., 2001. Monitoring land at regional and national scales and the role of remote sensing. *Int. J. Appl. Earth Obs. Geoinf.* 3, 162–175.
- Fang, Z., et al., 2019. Investigation into the differences among several outdoor thermal comfort indices against field survey in subtropics. *Sustain. Cities Soc.* 44, 676–690.
- Gál, C.V., Kántor, N., 2020. Modeling mean radiant temperature in outdoor spaces, a comparative numerical simulation and validation study. *Urban Clim.* 32, 100571.
- Gao, S., Zhan, Q., Yang, C., Liu, H., 2020. The diversified impacts of urban morphology on land surface temperature among urban functional zones. *Int. J. Environ. Res. Public Health.* <https://doi.org/10.3390/ijerph17249578>.
- Giannaros, C., Nenes, A., Giannaros, T.M., Kourtidis, K., Melas, D., 2018. A comprehensive approach for the simulation of the Urban Heat Island effect with the WRF/SLUCM modeling system: The case of Athens (Greece). *Atmos. Res.* 201, 86–101.
- Gorelick, N., et al., 2017. Google Earth Engine: planetary-scale geospatial analysis for everyone. *Remote Sens. Environ.* 202, 18–27.
- Grimm, N.B., et al., 2008. Global change and the ecology of cities. *Science* 319, 756–760.
- Gu, J., Qi, L., Zhou, S., Yan, X.J.S., 2016. Origins and review of urban time-space structure studies. *World Reg.* 25, 69–79.
- Gwet, K.L., 2008. Computing inter-rater reliability and its variance in the presence of high agreement. *Br. J. Math. Stat. Psychol.* 61, 29–48.
- Hay Chung, L.C., Xie, J., Ren, C., 2021. Improved machine-learning mapping of local climate zones in metropolitan areas using composite Earth observation data in Google Earth Engine. *Build. Environ.* 199, 107879.
- He, Q., Tan, S., Yin, C., Zhou, M., 2019. Collaborative optimization of rural residential land consolidation and urban construction land expansion: a case study of Huangpi in Wuhan, China. *Comput. Environ. Urban Syst.* 74, 218–228.
- Heiden, U., et al., 2012. Urban structure type characterization using hyperspectral remote sensing and height information. *Landsc. Urban Plan.* 105, 361–375.
- Hendel, M., Azos-Díaz, K., Tremeac, B., 2017. Behavioral adaptation to heat-related health risks in cities. *Energ. Buildings* 152, 823–829.
- Huang, H., et al., 2017. Mapping major land cover dynamics in Beijing using all Landsat images in Google Earth Engine. *Remote Sens. Environ.* 202, 166–176.
- Huang, J., Cedeno-Laurent, J.G., Spengler, J.D., 2014. CityComfort+: a simulation-based method for predicting mean radiant temperature in dense urban areas. *Build. Environ.* 80, 84–95.
- Issakov, A., Abylkassymova, A., 2024. Assessment of the dispersion of pollutants from automobile exhaust, taking into account relative humidity, pavement temperature, wind direction and speed, which varies depending on the time of day. *Int. Commun. Heat Mass Transfer* 159, 108140.
- Jamei, Y., Rajagopalan, P., Sun, Q., 2019. Spatial structure of surface urban heat island and its relationship with vegetation and built-up areas in Melbourne, Australia. *Sci. Total Environ.* 659, 1335–1351.
- Jie, P., et al., 2023. Impact of urban wind environment on urban building energy: a review of mechanisms and modeling. *Build. Environ.* 245, 110947.
- Kafy, A.A., et al., 2022. Predicting the impacts of land use/land cover changes on seasonal urban thermal characteristics using machine learning algorithms. *Build. Environ.* 217, 109066.
- Kusaka, H., Kondo, H., Kikegawa, Y., Kimura, F., 2001. A simple single-layer urban canopy model for atmospheric models: comparison with multi-layer and slab models. *Bound.-Lay. Meteorol.* 101, 329–358.
- Lambin, E.F., 2001. In: International Encyclopedia of the Social & Behavioral Sciences. Pergamon, Oxford, pp. 13150–13155.
- Lemonsu, A., Beaulant, A.L., Somot, S., Masson, V., 2014. Evolution of heat wave occurrence over the Paris basin (France) in the 21st century. *Clim. Res.* 61, 75–91.
- Li, J., Li, C., Zhu, F., Song, C., Wu, J., 2013. Spatiotemporal pattern of urbanization in Shanghai, China between 1989 and 2005. *Landsc. Ecol.* 28, 1545–1565.
- Li, H., Lin, J., Lei, X., Wei, T., 2022. Compressive strength prediction of basalt fiber reinforced concrete via random forest algorithm. *Mater. Today Commun.* 30, 103117.
- Li, X.-X., Liu, X., 2021. Effect of tree evapotranspiration and hydrological processes on urban microclimate in a tropical city: a WRF/SLUCM study. *Urban Clim.* 40, 101009.
- Li, F., Yigitcanlar, T., Nepal, M., Nguyen, K., Dur, F., 2023. Machine learning and remote sensing integration for leveraging urban sustainability: a review and framework. *Sustain. Cities Soc.* 96, 104653.
- Lin, J., Qiu, S., Tan, X., Zhuang, Y., 2023. Measuring the relationship between morphological spatial pattern of green space and urban heat island using machine learning methods. *Build. Environ.* 228, 109910.
- Liu, X., et al., 2018. High-resolution multi-temporal mapping of global urban land using Landsat images based on the Google Earth Engine Platform. *Remote Sens. Environ.* 209, 227–239.
- Liu, X., Li, X.-X., Harshan, S., Roth, M., Velasco, E., 2017. Evaluation of an urban canopy model in a tropical city: the role of tree evapotranspiration. *Environ. Res. Lett.* 12, 094008.
- Logan, T.M., Zaichik, B., Guikema, S., Nisbet, A., 2020. Night and day: The influence and relative importance of urban characteristics on remotely sensed land surface temperature. *Remote Sens. Environ.* 247, 111861.
- Ma, X., Zhang, L., Zhao, J., Wang, M., Cheng, Z., 2021. The outdoor pedestrian thermal comfort and behavior in a traditional residential settlement – a case study of the cave dwellings in cold winter of China. *Sol. Energy* 220, 130–143.
- McRae, I., et al., 2020. Integration of the WUDAPT, WRF, and ENVI-met models to simulate extreme daytime temperature mitigation strategies in San Jose, California. *Build. Environ.* 184, 107180.
- Mentes, Y., Yilmaz, S., Qaid, A., 2024. The cooling effect of different scales of urban parks on land surface temperatures in cold regions. *Energ. Buildings* 308, 113954.
- Mills, G., 2007. Cities as agents of global change. *Int. J. Climatol. (UK)* 27, 1849–1857.
- Mughal, M.O., Li, X.-X., Norford, L.K., 2020. Urban heat island mitigation in Singapore: evaluation using WRF/multilayer urban canopy model and local climate zones. *Urban Clim.* 34, 100714.
- Musy, M., Malys, L., Morille, B., Inard, C., 2015. The use of SOLENE-microclimat model to assess adaptation strategies at the district scale. *Urban Clim.* 14, 213–223.
- Nagendra, H., Bai, X., Brondizio, E.S., Lwasa, S., 2018. The urban south and the predicament of global sustainability. *Nat. Sustain.* 1, 341–349.
- Ngarambe, J., Oh, J.W., Su, M.A., Santamouris, M., Yun, G.Y., 2021. Influences of wind speed, sky conditions, land use and land cover characteristics on the magnitude of the urban heat island in Seoul: an exploratory analysis. *Sustain. Cities Soc.* 71, 102953.
- Nikolopoulou, M., Lykoudis, S., 2006. Thermal comfort in outdoor urban spaces: analysis across different European countries. *Build. Environ.* 41, 1455–1470.
- Ono, M., Tonouchi, M., 2014. Estimation of wet-bulb globe temperature using generally measured meteorological indices. *J. Biometeorol.* 50, 147.
- Parsons, K., 2006. Heat stress standard ISO 7243 and its global application. *Ind. Health* 44, 368–379.
- Peng, J., et al., 2024. Response of urban green space cooling effect to urbanization in the Three Ring Road area of Changsha City. *Sustain. Cities Soc.*, 105534.
- Powers, J.G., 2007. Numerical prediction of an Antarctic severe wind event with the weather research and forecasting (WRF) model. *Mon. Weather Rev.* 135, 3134–3157.
- Puissant, A., Weber, C., 2002. The utility of very high spatial resolution images to identify urban objects. *Geocarto Int.* 17, 33–44.
- Ren, C., et al., 2019. Assessment of local climate zone classification maps of cities in China and feasible refinements. *Sci. Rep.* 9, 18848.

- Ryu, Y.-H., Bou-Zeid, E., Wang, Z.-H., Smith, J.A., 2016. Realistic representation of trees in an urban canopy model. *Bound.-Lay. Meteorol.* 159, 193–220.
- Salata, F., Golasi, I., de Lieto Vollaro, R., de Lieto Vollaro, A., 2016. Urban microclimate and outdoor thermal comfort. A proper procedure to fit ENVI-met simulation outputs to experimental data. *Sustain. Cities Soc.* 26, 318–343.
- Sharma, M., Kumar, A., Supriya, M., Singh, V., Kishore, S., 2023. In: *Atmospheric Remote Sensing*. Elsevier, pp. 413–428.
- Sharmin, T., Steemers, K., Matzarakis, A., 2017. Microclimatic modelling in assessing the impact of urban geometry on urban thermal environment. *Sustain. Cities Soc.* 34, 293–308.
- Shi, M., Chen, M., Jia, W., Du, C., Wang, Y., 2023. Cooling effect and cooling accessibility of urban parks during hot summers in China's largest sustainability experiment. *Sustain. Cities Soc.* 93, 104519.
- Simwanda, M., Ranagalage, M., Estoque, R.C., Murayama, Y., 2019. Spatial analysis of surface urban heat islands in four rapidly growing African Cities. *Remote Sens.* (Basel). <https://doi.org/10.3390/rs11141645>.
- Skamarock, W., Klemp, J., Dudhia, J., Gill, D. O., Liu, Z., Berner, J., Wang, W., Powers, J. G., Duda, M. G., Barker, D., Huang, X.-Y., 2019. Description of the Advanced Research WRF Model Version 4.1. <https://doi.org/10.5065/1dfh-6p97> (No. NCAR/TN-556+STR).
- Smithson, C., Adams, B.R., 2024. Use of LCZs with urban canopy modeling to evaluate urban growth effects on meteorological conditions in the Salt Lake Valley. *Urban Clim.* 57, 102106.
- Stewart, I.D., Oke, T.R., 2012. Local climate zones for urban temperature studies. *Bull. Am. Meteorol. Soc.* 93, 1879–1900.
- Sun, X., et al., 2020. Quantifying landscape-metrics impacts on urban green-spaces and water-bodies cooling effect: the study of Nanjing, China. *Urban For. Urban Greening* 55, 126838.
- Tan, J., et al., 2024. Investigating the cooling effects of land cover and landscape patterns surrounding rivers: Insights from the subtropical city of Changsha, China. *Urban Clim.* 55, 101975.
- Teimori, G., et al., 2020. Applicability of the model presented by Australian Bureau of Meteorology to determine WBGT in outdoor workplaces: a case study. *Urban Clim.* 32, 100609.
- Tseliou, A., Tsiroi, I.X., Lykoudis, S., Nikolopoulou, M., 2010. An evaluation of three biometeorological indices for human thermal comfort in urban outdoor areas under real climatic conditions. *Build. Environ.* 45, 1346–1352.
- Vinayak, B., Lee, H.S., Gedam, S., Latha, R., 2022. Impacts of future urbanization on urban microclimate and thermal comfort over the Mumbai metropolitan region, India. *Sustain. Cities Soc.* 79, 103703.
- Wang, R., et al., 2019. Detecting multi-temporal land cover change and land surface temperature in Pearl River Delta by adopting local climate zone. *Urban Clim.* 28, 100455.
- Wang, A., et al., 2023. Ventilation analysis of urban functional zoning based on circuit model in Guangzhou in winter, China. *Urban Clim.* 47.
- Wang, R., Gao, W., Zhou, N., Kammen, D.M., Peng, W., 2021. Urban structure and its implication of heat stress by using remote sensing and simulation tool. *Sustain. Cities Soc.* 65, 102632.
- Wang, X., Scott, C.E., Dallimer, M., 2023. High summer land surface temperatures in a temperate city are mitigated by tree canopy cover. *Urban Clim.* 51, 101606.
- Wang, R., Voogt, J., Ren, C., Ng, E., 2022. Spatial-temporal variations of surface urban heat island: an application of local climate zone into large Chinese cities. *Build. Environ.* 222, 109378.
- Wang, A., Zhang, M.M., Chen, E.Q., Zhang, C., Han, Y.J., 2024. Impact of seasonal global land surface temperature (LST) change on gross primary production (GPP) in the early 21st century. *Sustain. Cities Soc.* 110.
- Weng, Q., 2012. Remote sensing of impervious surfaces in the urban areas: requirements, methods, and trends. *Remote Sens. Environ.* 117, 34–49.
- Weng, Q., Yang, S., 2004. Managing the adverse thermal effects of urban development in a densely populated Chinese city. *J. Environ. Manage.* 70, 145–156.
- Wu, Y., et al., 2022. Effects of landscape patterns on the morphological evolution of surface urban heat island in Hangzhou during 2000–2020. *Sustain. Cities Soc.* 79, 103717.
- Wu, J., Wu, N., 2023. Spatial structure and evolutionary logic of urban agglomerations based on remote sensing data. *Phys. Chem. Earth Parts A/B/C* 132, 103478.
- Wu, H., Ye, L.-P., Shi, W.-Z., Clarke, K.C., 2014. Assessing the effects of land use spatial structure on urban heat islands using HJ-1B remote sensing imagery in Wuhan, China. *Int. J. Appl. Earth Obs. Geoinf.* 32, 67–78.
- Xu, C., et al., 2012. Temporal variation of characteristic scales in urban landscapes: an insight into the evolving internal structures of China's two largest cities. *Landscape Ecol.* 27, 1063–1074.
- Xu, C., Huang, G.L., Zhang, M.M., 2024. Comparative analysis of the seasonal driving factors of the urban heat environment using machine learning: evidence from the wuhan urban agglomeration, China, 2020. *Atmosphere* 15.
- Xu, Y., Knudby, A., Shen, Y., Liu, Y., 2018. Mapping monthly air temperature in the Tibetan plateau from MODIS data based on machine learning methods. *IEEE J. Sel. Top. Appl. Earth Obs. Remote Sens.* 11, 345–354.
- Xu, D., Zhou, D., Wang, Y., Xu, W., Yang, Y., 2019. Field measurement study on the impacts of urban spatial indicators on urban climate in a Chinese basin and static-wind city. *Build. Environ.* 147, 482–494.
- Yang, F., et al., 2024. Evaluating the multi-seasonal impacts of urban blue-green space combination models on cooling and carbon-saving capacities. *Build. Environ.* 266, 112045.
- Zhang, X., et al., 2020. Modelling urban meteorology with increasing refinements for the complex morphology of a typical Chinese city (Xi'an). *Build. Environ.* 182, 107109.
- Zhang, M.M., et al., 2023. Impact of urban expansion on land surface temperature and carbon emissions using machine learning algorithms in Wuhan, China. *Urban Clim.* 47.
- Zhang, M.M., Tan, S.K., Liang, J.S., Zhang, C., Chen, E.Q., 2024. Predicting the impacts of urban development on urban thermal environment using machine learning algorithms in Nanjing, China. *J. Environ. Manage.* 356.
- Zhang, M.M., Tan, S.K., Zhang, C., Chen, E.Q., 2024. Machine learning in modelling the urban thermal field variance index and assessing the impacts of urban land expansion on seasonal thermal environment. *Sustain. Cities Soc.* 106.
- Zhang, Q., Zhou, D., Xu, D., Rogora, A., 2022. Correlation between cooling effect of green space and surrounding urban spatial form: Evidence from 36 urban green spaces. *Build. Environ.* 222, 109375.
- Zhang, Q., Zhou, D., Xu, D., Cheng, J., Rogora, A., 2022. Influencing factors of the thermal environment of urban green space. *Heliyon* 8, e11559.
- Zhao, C., Jensen, J., Weng, Q., Currit, N., Weaver, R., 2019. Application of airborne remote sensing data on mapping local climate zones: cases of three metropolitan areas of Texas. *U.S. Comput. Environ. Urban Syst.* 74, 175–193.
- Zhou, X., et al., 2022. Exploring the impacts of heat release of vehicles on urban heat mitigation in Sendai, Japan using WRF model integrated with urban LCZ. *Sustain. Cities Soc.* 82, 103922.
- Zhu, Y., et al., 2007. Evaluation of coupled outdoor and indoor thermal comfort environment and anthropogenic heat. *Build. Environ.* 42, 1018–1025.